行政院國家科學委員會補助專題研究計畫期末進度報告

（計畫名稱）**粒徑分布對具有布朗運動現象膠體的過濾與吸附行為的影響探討** (3/3)

計畫類別：■**個別型計畫**　　□ 整合型計畫

計畫編號：NSC　**96-2221-E-029-014-MY3**

執行期間：96 年　8 月　1 日至　99　年　7　月　31　日

計畫主持人：**張有義教授**

共同主持人：

計畫參與人員：

成果報告類型(依經費核定清單規定繳交)：□**精簡報告**■完整報告

本成果報告包括以下應繳交之附件：

□赴國外出差或研習心得報告一份

□赴大陸地區出差或研習心得報告一份

□**出席國際學術會議心得報告及發表之論文各一份**

□國際合作研究計畫國外研究報告書一份

處理方式：除產學合作研究計畫、提升產業技術及人才培育研究計畫、列管計畫及下列情形者外，得立即公開查詢

□涉及專利或其他智慧財產權，□一年□二年後可公開查詢

執行單位：台中市東海大學化工系

中　華　民　國　　99　年　　9　月　　日

期末報告

粒徑分布對具有布朗運動現象膠體的過濾與吸附行為的影響探討 (3/3)

NSC 96-2221-E-029-014-MY3

張有義教授

台中市東海大學化工系

中文摘要

本年度的研究內容主要在以動態模擬方法探討布朗運動行為對膠體在楔型管中（constricted tube model）吸附行為影響的探討。除了考慮布朗運動行為的影響外，本年度的研究在模擬過程中也考慮了下列三項變數的影響：1. 兩種不同楔型管的管壁形狀：拋物線型的管壁形狀（PCT）和正弦函數型的管壁形狀（SCT），2. DLVO 理論的作用能障，3. 流體剪切力對膠體吸附和脫附效應的影響。當不考慮脫附效應時，模擬結果發現在 PCT 中，在相同的 DLVO 作用力下，膠體的布朗運動行為會降低其吸附效率值。當流體流速增加時，由於膠體會傾向吸附在靠近 PCT 的中央最窄處，故其吸附效率值會隨之減少。但是在 SCT 中，在相同的 DLVO 作用力下，膠體的布朗運動行為只會稍為減少它們的吸附效率值。當考慮脫附效應時，相同的結果也會在 PCT 和 SCT 中得到，但膠體多層吸附的層數僅會達到第 3 層或第 4 層，且無法得到完全堵塞孔道的結果。

關鍵字：布朗運動；膠體；過濾；吸附行為。

English Abstract

With/without considering the detachment mechanism, the deposition morphology of Brownian/non-Brownian particles within a constricted tube is investigated by applying the Brownian dynamics simulation method in the present paper. Two different geometric structures, the parabolic constricted tube (PCT) and the sinusoidal constricted tube (SCT), are adopted. The effects of various types of the total interaction energy curves of the Derjaguin-Landau-Verwey-Overbeek (DLVO) theory and increasing flow velocity on the particle deposition morphology are also examined. For PCT without considering the detachment mechanism, under the same interaction energy curve, it is found that the number of non-Brownian particles deposited is higher than that of the Brownian particles. Since the deposition location moves closer to the constriction part of the tube, the number of

Brownian/non-Brownian particles increase with the decrease of flow velocity. The SCT behaves differently, it is found that the number of non-Brownian particles deposited is only slightly higher than that of Brownian particles. When the detachment mechanism is considered, same variation tendency is observed for those non-Brownian/Brownian particles within a PCT/SCT with the increase of the flow velocity. When comparing with the deposition morphology between PCT and SCT, it is found that a more uniform dendrite of 3 or 4 layers can be formed on the tube walls of PCT than that of SCT. The joint of individual dendrites at the blockage stage is not observed for both PCT and SCT in the present simulation.

Key Words：Brownian motion；colloid；filtration；deposition。

1. Introduction

In the deep bed filtration, since the amount of particles deposited on the surfaces of granular collectors and the corresponded structures of dendritic formations change with time, hence the morphology of the particle deposits changes continuously during the filtration period and affects the filter's ability to collect particles consequently. By using the method of trajectory analysis, Wang et al. [1] and Beizaie et al. [2] were the pioneers successfully established a direct approach for analyzing the deposition morphology of particles from a flowing suspension onto a spherical collector. In their approach, they had considered the deposition process as an interplay of two basic concepts, the shadow effect caused by those deposited particles and the random distribution of particles in the suspension, which are intrinsic to all of those particles deposited onto the granular surfaces. Their simulation procedure can be found in detail elsewhere [3] and will be adopted in the present paper. Then, by applying the concept of the control window located far upstream from a spherical collector, Ramarao et al. [4] successfully determine the collection efficiency of aerosols onto a spherical collector by using the method of Brownain dynamics simulation [5, 6]. The

simulation results obtained by Beizaie et al. [2] and Ramarao et al. [4] indicate that the deposition process consists of two consequence stages: the stage of decreasing porosity and the stage of blocking. In the first stage, the particle deposition occurs mainly through the individual adhesion, and a relatively smooth deposit layer will be formed on the grain surfaces. The major effect of deposition at this stage is to increase the effective grain dimension (or reduce the effective radius of the constricted tube shown below). The second stage of deposition is dominated by the blockage of the pore; particle deposition at this stage only resulting in the pore blockage, not in an increased grain diameter. Moreover, the lengths of these two stages were found to be dependent on the relative particle to collector size, the flow field around the collector and the relative magnitudes between the van der Waals attractive forces and the electrostatic repulsion forces of the Derjaguin-Landau-Verwey-Overbeek (DLVO) theory [7].

In our previous papers [8], with the consideration of the particle attachment mechanism only, we had investigated the deposition morphologies and the corresponded collection efficiencies of hydrosols onto a spherical collector. By using the same Brownian dynamics simulation method developed by Ramarao et al. [4] and including the shadow area effect cast by those deposited particles, the effect of various types of the total interaction energy curves of DLVO theory on the particles' collection efficiencies were examined in that paper. Comparing with the case without considering the Brownian diffusion force in the trajectory equation, our simulation results showed that the collection efficiency is always higher when the particle's Brownian motion behavior is taken into consideration. However, the detachment mechanism of particles was not considered in that paper.

Particle detachment resulting from fluid flowing through granular media has significant importance in many engineering fields such as filters. In the filtration

process, particle detachment and subsequent mobilization (i.e. reentrainment) may facilitate those particles to transport through the porous media and result in permeability reduction and high effluent turbidity. By adding a term of describing the reentrainment rate (i.e. first order proportional to the number of deposited particles) in the boundary condition at the collector surface, Dahneke [9] and Yoshida and Tien [10] were the pioneers to analysis the possibility of particle detachment in a deep bed filtration under the unfavorable surface interactions (i.e. with the presence of the electric repulsion energy barrier of the DLVO theory). Choo and Tien [11] proved experimentally that there is a critical detachment velocity existed in the second blockage stage, beyond which the attachment of particles becomes impossible. In their analyses, the equation of describing the effective pore radius caused by those deposited particles was adopted to calculate the collection efficiency during the different deposition stages. Ryan and Elimelech [12] also provided an excellent review on the fundamental detachment concept for the mobilization of colloids in groundwater. Later on, based on the hypothesis that the detachment of particles occurs when the hydrodynamic shear force overcomes the depth of the primary minimum of the DLVO theory, Bergendahl and Grasso [13, 14] had successfully established a predictive detachment model when the constricted tube model was adopted. Recently, Li et al. [15] and Johnson et al. [16] had experimentally discussed the role of hydrodynamic drag on the colloidal deposition and reentrainment in porous media under both favorable and unfavorable surface interaction conditions.

In the present paper, by applying with the equation describing the effective radius of the pore caused by those deposited particles [11], the deposition morphology of Brownian/non-Brownian particles within a constricted tube will be investigated with/without considering the detachment mechanism. Two different geometric structures, namely the parabolic constricted tube (PCT) and the sinusoidal constricted

tube (SCT), will be adopted. In these simulations, the effects of two different shapes of the total interaction energy curves of DLVO theory and increasing flow velocity are also considered. Distinguished deposition morphology is found between those particles with and without considering the particle's detachment mechanism.

2. The constricted tube model

Different from other models, for example, the capillary tube model [17, 18], the single sphere model [19, 20, 21] and the sphere-in-cell model [22], the constricted tube model is the only model takes the joint effect of neighboring grains and the blockage phenomenon caused by those deposited particles into consideration. The details of mathematic formulations describe this constricted tube model were provided in the excellent dissertation of Prof. Payatakes [23] and in the good review paper of Tien and Payatakes [24]. As shown in Fig. 1, the dimension of the constricted tube (i.e. PCT) is characterized by three quantities: the height, h, the maximum diameter, d_{max}, and the constriction diameter, d_c. The radius r_c and r_{max} are $d_c/2$ and $d_{max}/2$, respectively. Expressions for the determination of these quantities are summarized in Table 1. For a spherical collector with diameter d_f, the relationship between r_c, r_{max} and d_f are defined as (see chapter 3 in ref. [3]):

$$r_c = \frac{d_c}{2} = \frac{1}{2}\frac{\langle d_c \rangle}{\langle d_f \rangle} d_f \qquad (1)$$

$$r_{\max} = \frac{d_{\max}}{2} = \frac{1}{2}\left[\frac{\varepsilon(1-S_{wi})\langle d_f^3 \rangle}{(1-\varepsilon)\langle d_c^3 \rangle}\right]^{1/3} d_f \qquad (2)$$

where ε denotes the porosity of porous media, $<d_f>$ and $<d_c>$ are the mean values of the diameter of spherical collectors and pore constrictions, respectively, and $<d_f^3>$ and $<d_c^3>$ are the mean values of d_f^3 and d_c^3, respectively. In Eq. (2), S_{wi} represents the fraction of the irreducible saturation of porous media, and its value is 0.111 for

glass bead collectors and 0.127 for sand grain collectors [25]. In the present study, the filtration bed is assumed to be packed with sand grains.

The parabolic geometric structure (PCT as parabolic constricted tube) and the sinusoidal geometric structure (SCT as sinusoidal constricted tube) used by Payatakes et al. [25] are adopted for the constricted tube model in the present study. The expressions of the wall radius r_w for PCT is:

$$r_w = r_c + 4(r_{\max} - r_c)\left(0.5 - \frac{z}{l_f}\right)^2 \quad (3)$$

and for SCT is:

$$r_w = \frac{r_c + r_{\max}}{2}\left[1 + \left(\frac{r_{\max} - r_c}{r_{\max} + r_c}\right)\cos\left(2\pi\frac{z}{l_f}\right)\right] \quad \text{for} \quad 0 < \frac{z}{l_f} < 1 \quad (4)$$

The difference between those two geometric structures is that the tube wall of PCT exhibits the highest slope at the entrance and the lowest slope at the constriction part of the tube, and *vice versa* for SCT. In the present study, the flow field equations established by Chow and Soda [26] and modified by Chiang and Tien [27] are adopted.

3. Brownian Dynamics Simulation

Similar to the previous papers of Ramarao et al. [4] and Chang et al. [8], the principle of trajectory analysis and the method of Brownian dynamics simulation are adopted in the present study to simulate the direct deposition mechanism of particles. Unlike the case of the isolated spherical collector as described in our previous paper [8], the control window at the inlet cross-sectional area of the constricted tube is shown in Fig. 1. In the simulation of the present paper, we assume that the distribution of the initial position (r_{in}, θ_{in}) of each particle is assigned by the random number generator within the inlet control window. Note that the inlet positions of particles are located at $0 < r_{in} < r_0$ and $0 < \theta_{in} < 2\pi$, at which r_0 is the radial distance beyond

which no particle can be placed at the tube inlet (or control window), and r_0 can be found to be

$$r_0 = \frac{d_{\max} - d_p}{2} \qquad (5)$$

With the consideration of 200 particles originated from this inlet control window and the specification of the flow fluid within the tube, the particle deposition morphology can be determined by integrating the Langevin type trajectory equation below.

4. The Langevin type trajectory equation

In the present paper, if the gravity force is ignored, the Langevin type trajectory equation describing the force balance on a Brownian particle with a diameter d_p can be written as [5, 6]:

$$m_p \frac{dv_p}{dt} = F_d + F_e + F_r = F_d + F_{Lo} + F_{DL} + F_r \qquad (6)$$

where m_p is the mass of the particle, v_p is the particle velocity vector and t is the time. The forces considered in the present paper are the drag force F_d, the DLVO interaction force F_e, which is sum of the London van der Waals attractive force F_{Lo} and the electric double layer repulsive force F_{DL} [7], and the random force F_r. The trajectory of a Brownian particle described by the above Langevin type equation can be obtained incrementally. Over a sufficiently short time interval, $0 < t < \Delta t$, the fluid velocities of u_r and u_z can be regarded as constant. Note that the value of the time step Δt adopted in the present paper remains as small as 10^{-6} sec, which is the same order of the momentum relaxation time (~ $1/\beta$) of the particle [5].

By substituting the expressions of those forces shown in Eq. (6), then the particle velocities in the normal and tangential directions can be represented, respectively, as (i.e., see chapters 5 and 8 in ref. [3])

in the normal direction

$$v_{pr} = v_{pr}(0) + [(\frac{f_r^m}{f_r^t})u_r - v_{pr}(0) - (\frac{A_{DLVO}}{f_r^t})](1 - e^{-\beta C_s f_r^t t}) + \int_0^t e^{-\beta C_s f_r^t (t-\tau)} A(\tau) d\tau \quad (7)$$

with

$$A_{DLVO} = \frac{1}{m_{pi}\beta C_s}(F_{Lo} + F_{DL}), \text{ and } \beta = \frac{6\pi\mu a_{pi}}{C_s m_{pi}}$$

in the tangential direction

$$v_{p\theta} = v_{p\theta}(0) + [(\frac{B\varsigma_2 F_1 + C\varsigma_2^2 F_2}{B\varsigma_2 + C\varsigma_2^2})u_\theta - v_{p\theta}(0)][1 - e^{-(\beta C_s / F_3)t}] + \int_0^t e^{-(\beta C_s / F_3)(t-\tau)} A(\tau) d\tau \quad (8)$$

where $v_{pr}(0)$ and $v_{p\theta}(0)$ are the initial velocities of particles in the normal and tangential directions, respectively, m_{pi} is the mass of the ith particle, μ is the viscosity of the fluid, C_s is the Cunningham correction factor, β is the friction coefficient per unit mass of the particle, and F_1, F_2, F_3, f_r^m and f_r^t are the hydrodynamic retardation factors of normal vector, drag force and shear vector, and their numerical values at different separation distances can be found in Tables 5.1 and 5.3 of ref. [3], and $A(t)$ represents a Gaussian white noise process in stochastic terms [4, 8]. In Eq. (8), ς_2 is the normal coordinate of the particle center, and B and C are the polynomial coefficients to represent the tangential component of the un-disturbed flow field u_θ in the proximity of the collector surface,

$$u_\theta = B\varsigma_2 + C\varsigma_2^2 \quad (9)$$

where the values of B and C are dependent on the geometry of the collector, and their evaluation method can be found in chapter 5.8 of ref. [3].

By substituting dr/dt for v_{pr}, then the trajectory equation describing the ith particle path in the normal direction can be expressed as

$$r_r = r_r(0) + [(\frac{f_r^m}{f_r^t})u_r - v_{pr}(0) - (\frac{A_{DLVO}}{f_r^t})](\frac{e^{-\beta C_s f_r^t t} - 1}{\beta C_s f_r^t}) + [(\frac{f_r^m}{f_r^t})u_r - (\frac{A_{DLVO}}{f_r^t})]t + \frac{1}{\beta C_s f_r^t}\int_0^t [1 - e^{-\beta C_s f_r^t (t-\tau)}]A(\tau)d\tau \quad (10)$$

Similarly, in the tangential direction,

$$r_\theta = r_\theta(0) + \frac{F_3}{C_s\beta}[(\frac{B\varsigma_2 F_1 + C\varsigma_2^2 F_2}{B\varsigma_2 + C\varsigma_2^2})u_\theta - v_{p\theta}(0)][e^{-(\beta C_s / F_3)t} - 1] + (\frac{B\varsigma_2 F_1 + C\varsigma_2^2 F_2}{B\varsigma_2 + C\varsigma_2^2})u_\theta t + \frac{F_3}{C_s\beta}\int_0^t e^{-(\beta C_s / F_3)(t-\tau)}A(\tau)d\tau \quad (11)$$

Once the initial position of the ith particle r_{pi} originated in the control window is known, its trajectory can be determined based on the above trajectory equations. When the separation distance between the particle and the collector surface (or the previous deposited particle) is smaller than the radius of this ith particle, then we assume that this ith particle is deposited in the present paper.

According to the DLVO theory [7], F_{LO} and F_{DL} shown in Eq. (6) can be expressed as:

$$F_{LO} = -\nabla\phi_{LO}, \quad F_{DL} = -\nabla\phi_{DL} \quad (12)$$

with

$$\phi_{LO} = -N_{LO}\left[\frac{2(H+1)}{H(H+2)} + \ln H - \ln(H+2)\right]$$

(with the unit of k_BT)

$$\phi_{DL} = N_{E1}\left\{N_{E2}\ln\left[\frac{1+\exp(-X)}{1-\exp(-X)}\right] + \ln[1-\exp(-2X)]\right\}$$

(with the unit of k_BT)

hence:

$$F_{LO} = -\frac{2A}{3r_p}\left[\frac{1}{(H^2+2H)^2}\right] \quad (13)$$

$$F_{DL} = \frac{2k_B T}{r_p} N_{E1} \left(N_{DL} e^{-N_{DL} H} \right) \left\{ \frac{N_{E2} - e^{-N_{DL} H}}{1 - e^{-2N_{DL} H}} \right\} \qquad (14)$$

where $H = \frac{h_s}{r_p}$, $N_{LO} = \frac{A}{6k_B T}$, $N_{DL} = \kappa r_p$, $X = N_{DL} H$, $N_{E1} = \frac{\nu r_p (\varphi_1^2 + \varphi_2^2)}{4k_B T}$,

$$N_{E2} = \frac{2\left(\frac{\varphi_1}{\varphi_2}\right)}{\left[1 + \left(\frac{\varphi_1}{\varphi_2}\right)^2\right]}.$$

In the above equation, r_p is the radius of the particle, h_s is the smallest separation distance between the particle and the collector surface, A is the Hamaker constant, k_B is the Boltzmann constant, T is the absolute temperature, κ is the reciprocal of the electric double layer thickness, ν is the dielectric constant of the fluid, and φ_1 and φ_2 are the surface (zeta) potentials of the particle and the tube wall, respectively. The algebraic sum of the van der Waals and double-layer potentials gives the total interaction energy curve of the DLVO theory (i.e. $V_T/k_BT=\phi_{LO}+\phi_{DL}$) [7]. In the present paper, the effects of two types of interaction energy curves [28] on the particle's deposition morphology will be investigated. As shown in Fig. 2, curves A exhibits a large primary maximum and a deep secondary minimum; while a "barrierless" interaction energy curve is represented by curve B. In this figure, N_{E1}=105.0 and N_{DL}=10.75 for curve A, N_{E1}=0.0 and N_{DL}=0.0 for curve B, and N_{E2}=1.0 and N_{L0} =7.0 for both curves. Corresponding to these two types of interaction energy curves with the defined values of N_{E1}, N_{E2}, N_{L0} and N_{DL}, the deposition morphology of Brownian/non-Brownian particles within a PCT/SCT will be given below.

5. The effective radius of the pore and the critical detachment velocity

Since the tube radius will be continuously reduced as particle deposition

proceeds, it becomes unrealistic when both the increased surface area provided by those deposited particles and the flow velocity changed effect are not considered. In the present paper, we will adopt the equation of the effective radius to solve this tube radius reduced problem in the first stage of deposition described above as follows.

If a layer of deposit is formed over the tube wall surfaces, the effective radius of the constricted tube can be assume to be as [11]

$$R = R_d + (R_0 - R_d)\left(\frac{z}{l}\right)^n \qquad (15)$$

with $R_d = \dfrac{-R_0 + \sqrt{R_0^2 - 4n\left(\dfrac{N_p}{6(1-\varepsilon_d)}\dfrac{(2n+1)(n+1)}{2nl}d_p^3 - R_0^2(n+1)\right)}}{2n}$

where R is the local radius of the tube, R_d is the value of R at the inlet of the tube, n is a constant, z is the tube axial distance measured from the inlet, l is the length of the tube, ε_d is the deposit porosity and N_p is the number of particles deposited. The choice of n is somewhat arbitrary; it can be chosen to give the best fit with experimental data, and is dependent on the ratio of particle diameter to grain diameter, N_R. With small N_R, the distribution of particle deposit tends to be more uniform leading to a larger value of n. On the contrary, with large N_R, particles will be deposited mostly near the tube inlet leading to a more nonuniform deposition and a smaller value of n. Choo and Tien [11] found that $n = 0.15$ when $v_c = 0.7$ cm/sec and $\varepsilon_d = 0.8$, and $n = 0.5$ when $v_c = 0.4$ cm/sec and $\varepsilon_d = 0.8$ can fit best to their experimental data. In the present paper, we will adopt the values of $n = 0.5$ when $v_c = 0.4$ cm/sec and $\varepsilon_d = 0.8$ to simulate the deposited morphology of particles when the detachment mechanism is considered.

The detachment mechanism requires a large tangential drag force acting on the depositing particle if the local fluid velocity in the tube is excessively large. Since the

deposition of particles continuous narrow the available cross-sectional area for flow, Choo and Tien [11] argued that there exists a critical velocity, v_c, beyond which particle deposition becomes impossible. One may estimate v_c by relating the tangential force F_θ as

$$F_\theta = 1.7005 \times 6\pi\mu a_p v_\theta \qquad (16)$$

where v_θ is the tangential velocity at a distance a_p from the surface of the deposit layer. If the critical velocity of $v_c = v_\theta = 0.4$ cm/sec is chosen, then a corresponding value of $F_\theta = 0.641 \times 10^{-10}\ N$ can be obtained with $a_p = 1.0\ \mu m$. Since this value of $F_\theta = 0.641 \times 10^{-10}\ N$ is greater than the maximum adhesive force of $0.187 \times 10^{-10}\ N$ obtained by Li et al. [15] when the constricted tube model was adopted (i.e. corresponding to the maximum drag torque of $1.27 \times 10^{-19}\ Nm$ with a lever arm length of 6.8 nm), hence we will assume that the particle's deposition is impossible when its tangential velocity is greater than the critical velocity of $v_\theta = 0.4$ cm/sec in the simulations of considering the detachment mechanism as follows.

6. Numerical Simulation and Results

6.1. The detachment mechanism is not considered

The deposition morphology obtained from the trajectory equations based on the above stochastic simulation procedures for those two type interaction energy curves shown in Fig. 2 are given below. The corresponding simulation parameters are presented in Table 1. The cases of considering and without considering the Brownian motion behavior of particles within a PCT/SCT when the detachment mechanism is not considered are illustrated below.

For U_{in}=0.2 cm/sec, the simulation results of the deposition morphology of Brownian/non-Brownian particles within PCT for the interaction energy curves A and B shown in Fig. 2 are illustrated in Fig. 3. Regardless whether the Brownian motion behavior of particles is considered or not, since there is no energy barrier existed in case B, hence the number of particles collected for curve B is always greater than that of curve A. More importantly, because of their increased ability to overcome the height of the energy barrier of curve A shown in Fig. 2, hence those Brownian particles are easier to deposit at the entrance region of the tube than the non-Brownian particles. On the contrary, since those particles without considering the Brownian motion behavior own smaller ability to overcome the energy barrier, and therefore are able to deposit at the region close to the center narrow part of the tube as shown in Fig. 1, so the number of particles deposited for non-Brownian particles are larger than those of the Brownian particles as shown in Fig. 3. Note that, for those non-Brownian particles, since they are easier to deposit at the center part of the tube, so they own greater opportunity to intercept those upcoming particles to form the multi-layer dendrites, and therefore the second blockage stage for those non-Brownian particles is easier to achieve at the constricted part than that at the entrance region of the tube.

When the flow velocity is decreased from U_{in}=0.2 cm/sec to U_{in}=0.1 cm/sec, the simulation results of the deposition morphology of Brownian/non-Brownian particles within PCT are shown in Fig. 4. Similar to those observed in Fig. 3, the order of the magnitude is curve B > curve A. Since those non-Brownian particles are easier to deposit at the constricted part of the tube, therefore the number of particles deposited for non-Brownian particles is always greater than those of the Brownian particles. Accompanying with the smaller inertia forces for U_{in}=0.1 cm/sec, since those upcoming non-Brownian/Brownian particles

originated from the tube inlet are easier to be intercepted by those already deposited particles, hence the number of particle deposited as shown in Fig. 4 where U_{in}=0.1 cm/sec is always greater than those results shown in Fig. 3 where U_{in}=0.2 cm/sec.

In order to investigate the effect of wall geometry on the number of non-Brownian/Brownian particles deposited and the corresponded deposition morphology, the geometric structure of the sinusoidal constricted tube (SCT) is also adopted in our simulations as follows. The number of particles deposited obtained by using the present dynamics simulation method for U_{in}=0.1 cm/sec and U_{in}=0.2 cm/sec in PCT and SCT are summarized in Table 2 and Table 3, respectively. Different with those results obtained by using PCT, it can be found that the number of non-Brownian particles is only slightly higher than that of Brownian particles when SCT is adopted. The number of non-Brownian/Brownian particles deposited also increases slightly when the flow velocity is decreased from U_{in}=0.2 cm/sec to U_{in} =0.1 cm/sec. The typical sets of the deposition morphology of Brownian/non-Brownian particles for curves A and B within SCT at U_{in}=0.1 cm/sec and U_{in}=0.2 cm/sec are illustrated in Figs. 5 and Figs. 6, respectively. When comparing the two geometric structures of PCT (see Figs. 3 or 4) and SCT (see Figs. 5 or 6), it can be found that the tube wall of PCT exhibits a higher slope at the entrance and a lower slope at the constriction part of the tube than that of SCT. Therefore, the flow fields corresponding to these two geometric structures are different. For example, for SCT, the streamlines at the entrance of the tube are parallel to the axial direction, and persist along that direction over a certain distance before they move toward the center of the tube. This puts particles in a more favorable

collection situation to deposit at the constriction part of SCT than that of PCT, at which the streamlines at the entrance are parallel to the axis, but change their direction very quickly as they move into the cell center [29]. In the simulations of using SCT, in addition to those factors of the flow rate and the DLVO interaction energy curves, we found that the steep slope of the tube wall near the constriction part of the tube dominates the whole deposition process of Brownian/non-Brownian particles. By this fact, as illustrated in Figs. 5 and 6, the joint of individual dendrites and therefore the second blockage stage becomes more pronounced in SCT.

6.2. The detachment mechanism is considered

In the above simulations, since the detachment mechanism of particles is not considered when the tangential drag force acting on the depositing particle is large enough, so those deposition morphologies of non-Brownian/Brownian particles illustrate in Figs. 3-6 become unrealistic. In the following simulations, the changed flow field corresponding to the Nth particle deposition is obtained from the effective radius equation obtained by using Eq. (15), and the detachment criteria of the (N+1)th particle is attained when its local tangential velocity is greater than the critical detachment velocity 0.4 cm/sec described above.

Fig. 7 shows the deposition morphology of non-Brownian/Brownian particles in PCT corresponding to curves A and B shown in Fig. 2 when U_{in}=0.2 cm/sec. Same as those observed in Fig. 3 that the number of particles deposited for the “barrierless” type curve B is higher than that of curve A where a large primary maximum and a deep secondary minimum existed. However, since the detachment mechanism is considered, there are only 3 or 4 layers can be formed in the multi-layer dendrites as shown in Figs. 7(a)-(d), and the number of non-Brownian particles deposited is almost the same as that of Brownian particles for the same interaction energy curve. Note that those Brownian particles still can form the multi-layer dendrites more close to the

entrance region than those non-Brownian particles. When the flow velocity is decreased from U_{in}=0.2 cm/sec to U_{in}=0.1 cm/sec as shown in Figs. 8(a)-(d), same as those obtained in Fig. 4, the number of particles deposited is always increased for either non-Brownian or Brownian particles. The maximum number of layers formed in the dendrites also increases to five. Note that a uniform deposition layer is observed for U_{in}=0.2 cm/sec (see Fig. 7), but a non-uniform deposition layer is observed for U_{in}=0.1 cm/sec (see Fig. 8).

Figs. 9(a)-(d) and 10(a)-(d) show the deposition morphology of non-Brownian/Brownian particles in SCT corresponding to curves A and B shown in Fig. 2 when U_{in}=0.1 cm/sec and U_{in}=0.2 cm/sec, respectively. Same as the above results for SCT, the number of non-Brownian/Brownian particles deposited for curve B is higher that that of curve A at the same flow velocity and the number of particles deposited decreases with the increase of the flow velocity for the same interaction energy curve. Because of its steep slope of the tube wall near the constricted part of the tube, the number of non-Brownian/Brownian particles deposited in SCT is also higher than that in PCT. When comparing the deposition morphology between PCT (see Figs. 3-6) and SCT (see Figs. 7-10), a more “concentrated” and non-uniform dendrite is observed to form at the region close to the center part of SCT. Even with the steep slope of the tube wall near the constricted part of tube, because of the detachment criteria is attained, the joint of individual dendrites at the blockage stage is not observed for SCT in the present simulation. The number of particles deposited in PCT and SCT obtained by the present case when the detachment mechanism is considered are summarized in Table 4 and Table 5 for U_{in}=0.1 cm/sec and U_{in}=0.2 cm/sec, respectively. Also, from the above deposition morphologies demonstrated in

both PCT and SCT, it can be found that particle deposition over the tube wall surfaces is hardly to occur at the second half of the tube.

7. Conclusion

By applying the Brownian dynamics simulation method, the deposition morphologies of non-Borwnian/Brownian particles within the constricted tube of two different geometric structures, PCT and SCT, for various types of the DLVO interaction energy curves have been studied. When the detachment mechanism is not considered, because of their ability to move closer to the constriction part of the tube, the number of non-Brownian particles deposited is always greater than those of Brownian particles. For PCT, the number of Brownian/non-Brownian particles increase significantly when the flow velocity is decreased from U_{in}=0.2 cm/sec to U_{in}=0.1 cm/sec. Because of the steep slope of the tube wall near the constriction part of the tube dominates the whole deposition process, the number of Brownian/non-Brownian particles deposited for SCT is greater than that of PCT. Same variation tendency is observed for those non-Brownian/Brownian particles within the PCT/SCT when the detachment mechanism is considered. Because of the attainment of the detachment criteria, not like the case without considering the detachment mechanism at which the joint of individual dendrites at the second blockage stage is obtained, there are only four and five layers can be formed in the multi-later dendrites in PCT and SCT, respectively, in the present study.

Acknowledgment

The authors would like to express their sincere thanks to Prof. Chi Tien at Chemical Engineering Department of Syracuse University for the valuable suggestion on the method of trajectory analysis of this work. The financial support received from the National Science Council of the Republic of China, research grant no. NSC-94-2214-E-029-003, is greatly appreciated.

References

[1] C.S. Wang, M. Beizaie, C. Tien, Deposition of Solid Particles in a Collector: Formation of a New Theory, AIChE J. 23 (1977) 879-889.

[2] M. Beizaie, C.S. Wang, C. Tien, A Simulation Model of Particle Deposition on Single Collectors, Chem. Eng. Commun. 13 (1981) 153-180.

[3] C. Tien, Granular filtration of aerosols and hydrosols, 2nd edition, Butterworths, Boston, 2007.

[4] B.V. Ramarao, C. Tien, S. Mohan, Calculation of Single Fiber Efficiencies for interception and Impaction with Superposed Brownian Motion, J. Aerosol Sci. 25 (1994) 295-313.

[5] C. Kanaoka, H. Emi, W. Tarthapanichakoon, Convective diffusional deposition and collection efficiency of aerosol on a dust-loaded fiber, AIChE J. 29 (1983) 895-902.

[6] D. Gupta, M.H. Peters, A Brownian dynamics simulation of aerosol deposition onto spherical collectors, J. Colloid Interface Sci. 104 (1985) 375-389.

[7] E.J.W. Verwey, J.Th.G. Overbeek, Theory of the stability of lyophobic colloids, Elsevier, Amsterdam, 1948.

[8] Y.I. Chang, R.S. Lee, W.Y. Cheng, The Deposition Morphology of Brownian particles onto a Spherical Collector, Separation and Purification Tech. 52 (2006) 126-135.

[9] B. Dahneke, Resuspension of particles, J. Colloid Interface Sci. 50 (1975) 194-196.

[10]. H. Yosida, C. Tien, Analysis of Brownian particle deposition and reentrainment in granular beds, J. Colloid Interface Sci. 111 (1986) 189-196.

[11] C. Choo, C. Tien, Simulation of hydrosol deposition in granular media, AIChE J. 41 (1995) 1426-1442.

[12] J. N. Ryan, M. Elimelech, Colloid mobilization and transport in groundwater, Colloids Surf. A: Physicochem. Eng., 107 (1996) 1-56.

[13] J.A. Bergendahl, D. Grasso, Prediction of colloid detachment in a model porous media: hydrodynamics. Chemical Eng. Sci., 55 (2000) 1523-1532.

[14] J.A. Bergendahl, D. Grasso, Mechanistic basis for particle detachment from granular media, Enviro. Sci. Technol., 37 (2003) 2317-2322.

[15] X. Li, P. F. Zhang, C. L. Lin, W. P. Johnson, Role of hydrodynamic drag on microsphere deposition and reentrainment in porous mdeia under unfavorable conditions, Environ. Sci. Technol., 39 (2005) 4012-4020.

[16] W.P. Johnson, X. Li, S. Assemi, Deposition and reentrainment dynamics of microbes and non-biological colloids during non-perturbed transport in porous media in the presence of an energy barrier to deposition. Adv. in Water Resources, 30 (2007) 1432-1454.

[17] A.C. Payatakes, R. Rajagopalan, C. Tien, Application of Porous Media Modelsto the Study of Deep Bed Filtration, Canadian J. Chem. Eng. 52 (1974) 722-731.

[18] C.C. Hung, C. Tien, Effect of Particle Deposition on the Reduction of Water Flux in Reverse Osmosis, Desalination 18 (1976) 173-187.

[19] K.M. Yao, M.T. Habidian, C.R. O'Melia, Water and waste water filtration: concepts and applications, Environ. Sci. Tech. 5 (1971), 1105-1112.

[20] L.A. Spielman, J.A. FitzPatrick, Theory for particle collection under London and gravity forces, J. Colloid Interface Sci. 42 (1973) 607-623.

[21] R. Rajagopalan, C. Tien, Single Collector Analysis of Collection Mechanisms in Water Filtration, Canadian J. Chem. Eng. 55 (1977) 246-255.

[22] R. Rajagopalan, C. Tien, Trajectory Analysis of Deep-Bed Filtration with Sphere-in-cell Porous Media Model, AIChE J. 22 (1976) 523-533.

[23] A.C. Payatakes, A new model for granular porous media, application to filtration through packed-beds, Ph.D. dissertation, Syracuse University, Syracuse, New York, 1973.

[24] C. Tien, A.C. Payatakes, Advances in deep bed filtration, AIChE J. 25 (1979) 737-759.

[25] A.C. Payatakes, C. Tien, R.M. Turian, A New Model of Granular Porous Media: Part-1 Model Formulation, AIChE J. 19 (1973) 58-66.

[26] J.C.F. Chow, K. Soda, Laminar flow in tubes with constriction, Physics of Fluids 15 (1972) 1701-1706.

[27] H.W. Chiang, C. Tien, Dynamics of Deep Bed Filtration: Part I. Analysis of Two Limiting Situations, AIChE J. 31 (1985) 1349-1359.

[28] J.S. Kim, R. Rajagopalan, Adsorption of Brownian Particles in the Presence of Potential Barriers: Effect of Different Modes of Double Layer Interaction, J. Colloid Interface Sci. 83 (1981) 428-448.

[29] Y.I. Chang, S.C. Chen, E. Lee, Prediction of Brownian Particle Deposition in Porous Media Using the Constricted Tube Model, J. Colloid Interface Sci. 266 (2003) 48-59.

Legends of Tables and Figures

Table 1. Parameter values adopted in the theoretical simulations of the present paper.

Table 2. The number of Brownian/non-Brownian particles deposited corresponding to the two DLVO interaction energy curves A and B shown in Fig. 2 for PCT when the detachment mechanism is not considered at U_{in} = 0.1 cm/sec and U_{in} = 0.2 cm/sec, respectively.

Table 3. The number of Brownian/non-Brownian particles deposited corresponding to the two DLVO interaction energy curves A and B shown in Fig. 2 for SCT when the

detachment mechanism is not considered at U_{in} = 0.1 cm/sec and U_{in} = 0.2 cm/sec, respectively.

Table 4. The number of Brownian/non-Brownian particles deposited corresponding to the two DLVO interaction energy curves A and B shown in Fig. 2 for PCT when the detachment mechanism is considered at U_{in} = 0.1 cm/sec and U_{in} = 0.2 cm/sec, respectively.

Table 5. The number of Brownian/non-Brownian particles deposited corresponding to the two DLVO interaction energy curves A and B shown in Fig. 2 for SCT when the detachment mechanism is not considered at U_{in} = 0.1 cm/sec and U_{in} = 0.2 cm/sec, respectively.

Figure 1. The schematic diagram of the control window for simulating deposition of Brownian particles within a constricted tube (i.e. PCT), in which the concept of shadow area is illustrated.

Figure 2. Two types of total interaction energy curves adopted in the simulation of the present paper, at which N_{E1}=105.0 and N_{DL}=10.75 for curve A, N_{E1}=0.0 and N_{DL}=0.0 for curve B, and N_{E2}=1.0 and N_{L0} =7.0 for both curves.

Figure 3. Simulations results of the deposition morphology of Brownian/non-Brownian particles within PCT for the interaction energy curves A and B shown in Fig. 2 without considering the detachment mechanism when $U_{in} = 0.2$ cm/sec: (a) Curve A for the non-Brownian particles; (b) Curve A for the Brownian particles; (c) Curve B for the non-Brownian particles; (d) Curve B for the Brownian particles.

Figure 4. Simulations results of the deposition morphology of non-Brownian/Brownian particles within PCT for the interaction energy curve B shown in Fig. 2 without considering the detachment mechanism when $U_{in} = 0.1$

cm/sec: (a) Curve A for the non-Brownian particles; (b) Curve A for the Brownian particles; (c) Curve B for the non-Brownian particles; (d) Curve B for the Brownian particles.

Figure 5. Simulations results of the deposition morphology of Brownian/non-Brownian particles within SCT for the interaction energy curves A and B shown in Fig. 2 without considering the detachment mechanism when $U_{in} = 0.1$ cm/sec: (a) Curve A for the non-Brownian particles; (b) Curve A for the Brownian particles; (c) Curve B for the non-Brownian particles; (d) Curve B for the Brownian particles.

Figure 6. Simulations results of the deposition morphology of Brownian/non-Brownian particles within SCT for the interaction energy curves A and B shown in Fig. 2 without considering the detachment mechanism when $U_{in} = 0.2$ cm/sec: (a) Curve A for the non-Brownian particles; (b) Curve A for the Brownian particles; (c) Curve B for the non-Brownian particles; (d) Curve B for the Brownian particles.

Figure 7. Simulations results of the deposition morphology of Brownian/non-Brownian particles within PCT for the interaction energy curves A and B shown in Fig. 2 with the consideration of the detachment mechanism when $U_{in} = 0.2$ cm/sec: (a) Curve A for the non-Brownian particles; (b) Curve A for the Brownian particles; (c) Curve B for the non-Brownian particles; (d) Curve B for the Brownian particles.

Figure 8. Simulations results of the deposition morphology of non-Brownian/Brownian particles within PCT for the interaction energy curves A and B shown in Fig. 2 with the consideration of the detachment mechanism when $U_{in} = 0.1$ cm/sec: (a) Curve A for the non-Brownian particles; (b) Curve A for the

Brownian particles; (c) Curve B for the non-Brownian particles; (d) Curve B for the Brownian particles.

Figure 9. Simulations results of the deposition morphology of Brownian/non-Brownian particles within SCT for the interaction energy curves A and B shown in Fig. 2 with the consideration of the detachment mechanism when $U_{in} = 0.1$ cm/sec: (a) Curve A for the non-Brownian particles; (b) Curve A for the Brownian particles; (c) Curve B for the non-Brownian particles; (d) Curve B for the Brownian particles.

Figure 10. Simulations results of the deposition morphology of Brownian/non-Brownian particles within SCT for the interaction energy curves A and B shown in Fig. 2 with the consideration of the detachment mechanism when $U_{in} = 0.2$ cm/sec: (a) Curve A for the non-Brownian particles; (b) Curve A for the Brownian particles; (c) Curve B for the non-Brownian particles; (d) Curve B for the Brownian particles.

Parameters	Values
k_B	1.38 x10^{-16} erg/K
T	293 K
ε	0.4
μ	1.0 cp
ρ_f	1.0 g/cm^3
ρ_p	1.0 g/cm^3
d_f	20 μ m
d_p	1.0 μ m
U_{in}	0.1~0.2 cm/sec
C_{in}	200 ppm

Table 1.

PCT (without considering the detachment mechanism)				
	U_{in}=0.1cm/s		U_{in}=0.2 cm/s	
Number of particles deposited	Curve A	Curve B	Curve A	Curve B
Brownian Particle	69	110	56	80
Non-Brownian Particle	83	120	60	92

Table 2.

SCT (without considering the detachment mechanism)				
	U_{in}=0.1cm/s		U_{in}=0.2 cm/s	
Number of particles deposited	Curve A	Curve B	Curve A	Curve B
Brownian Particle	74	128	68	124
Non-Brownian Particle	75	130	72	127

Table 3.

PCT (with the consideration of the detachment mechanism)				
	U_{in}=0.1cm/s		U_{in}=0.2 cm/s	
Number of particles deposited	Curve A	Curve B	Curve A	Curve B
Brownian Particle	28	38	24	36
Non-Brownian Particle	29	42	24	39

Table 4.

SCT (with the consideration of the detachment mechanism)				
	U_{in}=0.1cm/s		U_{in}=0.2 cm/s	
Number of particles deposited	Curve A	Curve B	Curve A	Curve B
Brownian Particle	40	56	30	56
Non-Brownian Particle	40	57	30	54

Table 5.

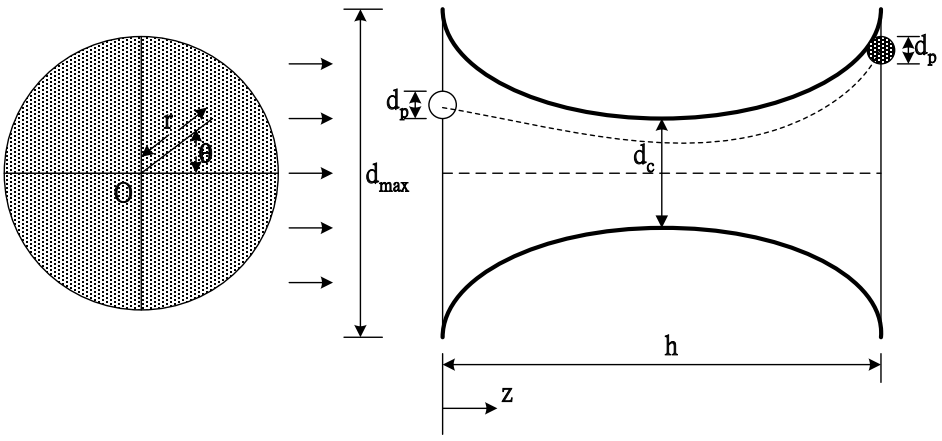

Fig. 1

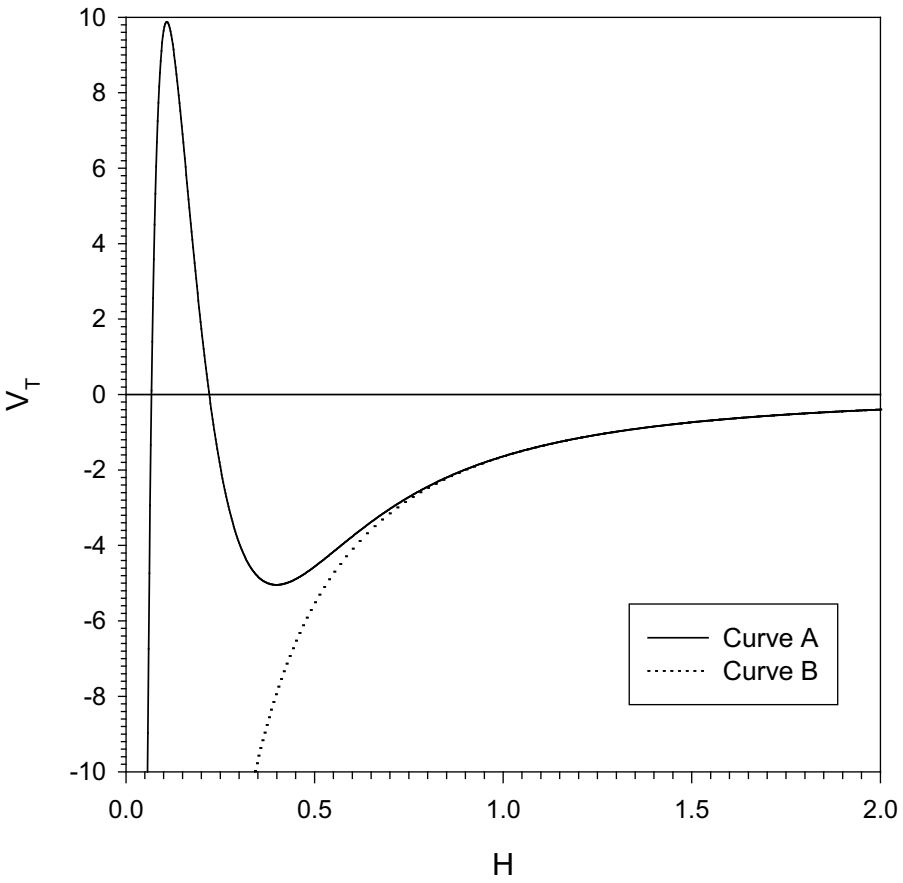

Fig. 2

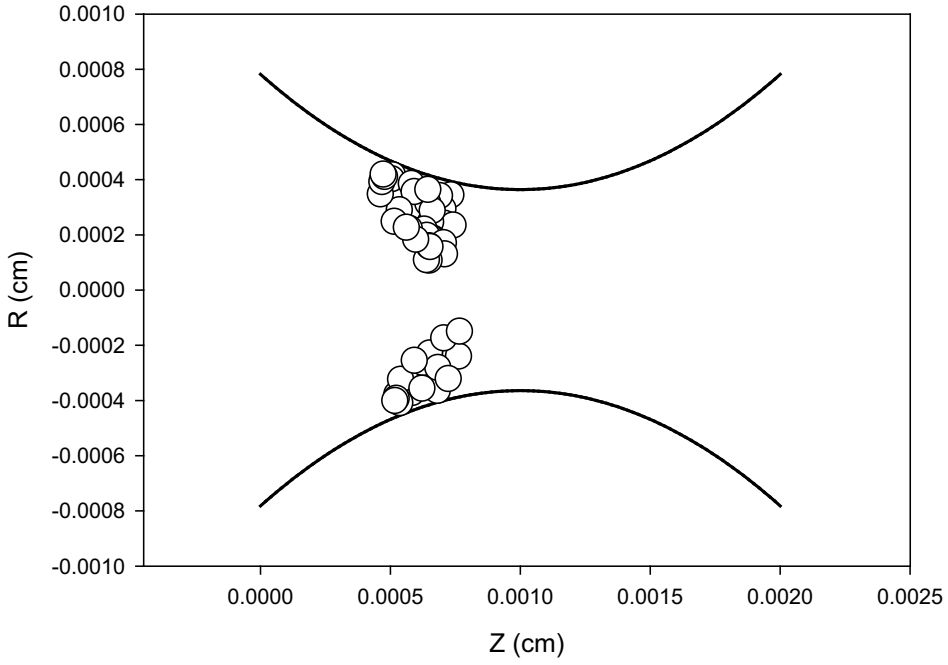
0.0010
0.0008
0.0006
0.0004
0.0002
0.0000
-0.0002
-0.0004
-0.0006
-0.0008
-0.0010
R (cm)
0.0000
0.0005
0.0010
0.0015
0.0020
0.0025
Z (cm)

Fig. 3(a)

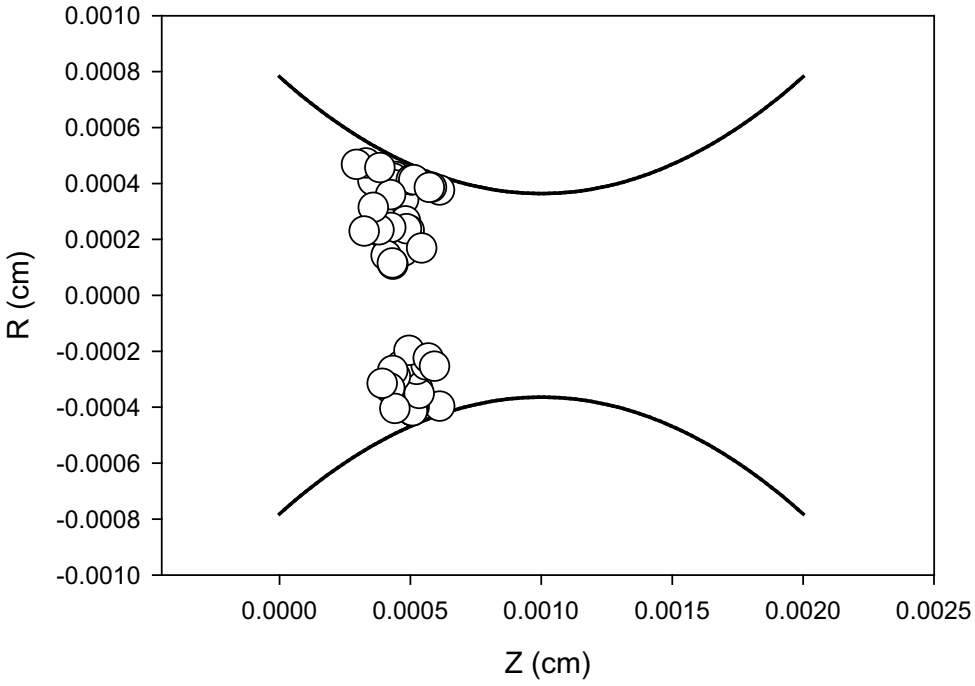
0.0010
0.0008
0.0006
0.0004
0.0002
0.0000
-0.0002
-0.0004
-0.0006
-0.0008
-0.0010
R (cm)
0.0000
0.0005
0.0010
0.0015
0.0020
0.0025
Z (cm)

Fig. 3(b)

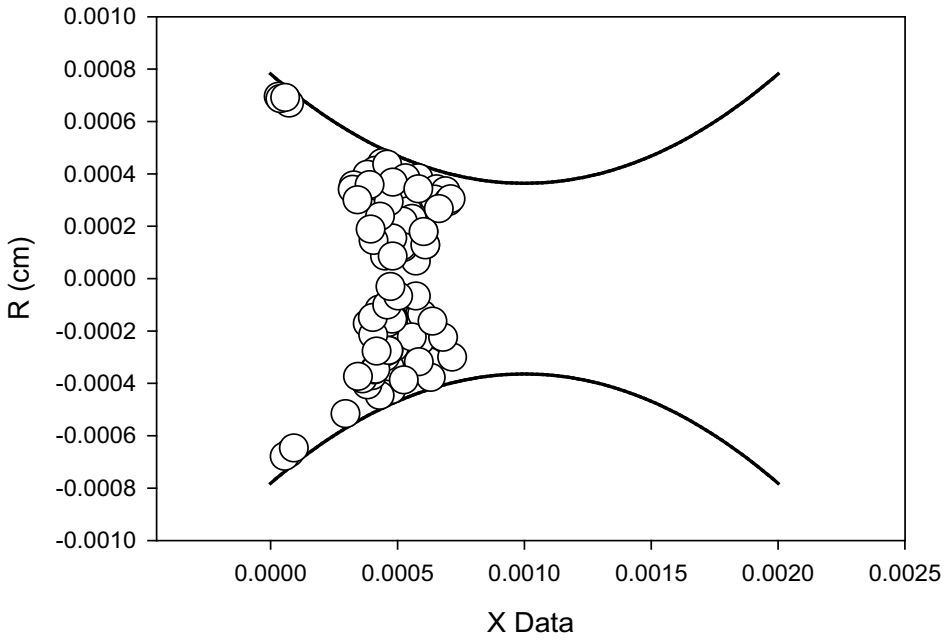
0.0010
0.0008
0.0006
0.0004
0.0002
0.0000
-0.0002
-0.0004
-0.0006
-0.0008
-0.0010
R (cm)
0.0000
0.0005
0.0010
0.0015
0.0020
0.0025
X Data

Fig. 3(c)

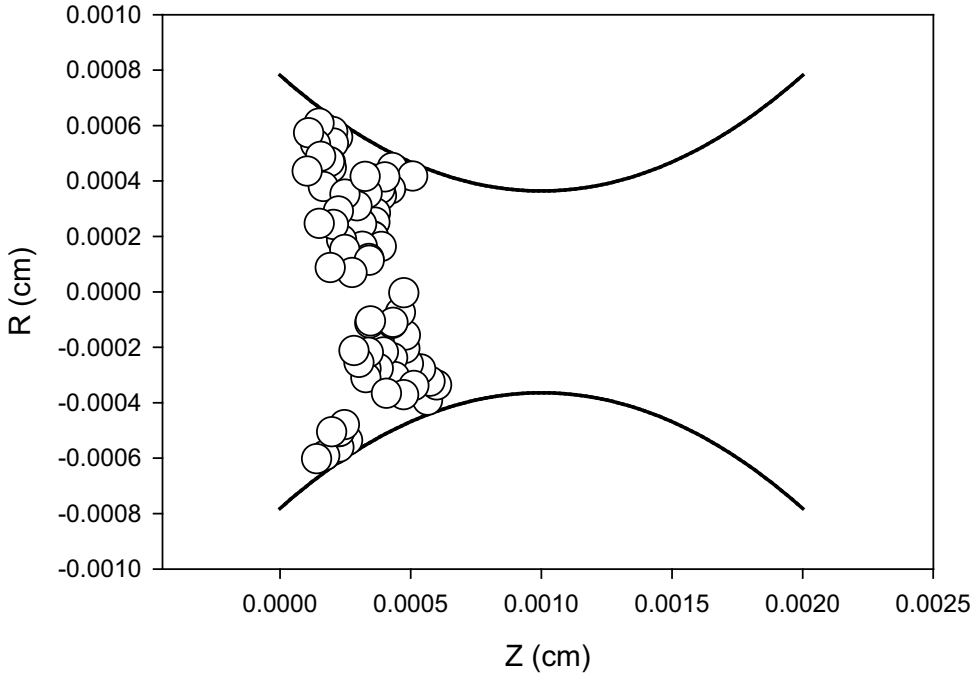
0.0010
0.0008
0.0006
0.0004
0.0002
0.0000
-0.0002
-0.0004
-0.0006
-0.0008
-0.0010
R (cm)
0.0000
0.0005
0.0010
0.0015
0.0020
0.0025
Z (cm)

Fig. 3(d)

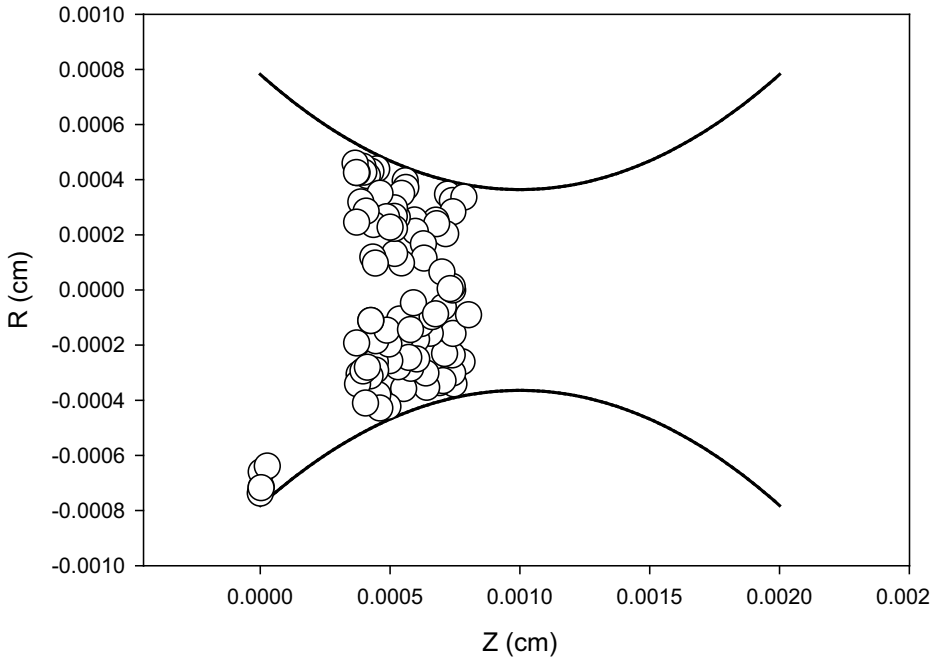
0.0010
0.0008
0.0006
0.0004
0.0002
0.0000
-0.0002
-0.0004
-0.0006
-0.0008
-0.0010
R (cm)
0.0000
0.0005
0.0010
0.0015
0.0020
0.002
Z (cm)

Fig. 4(a)

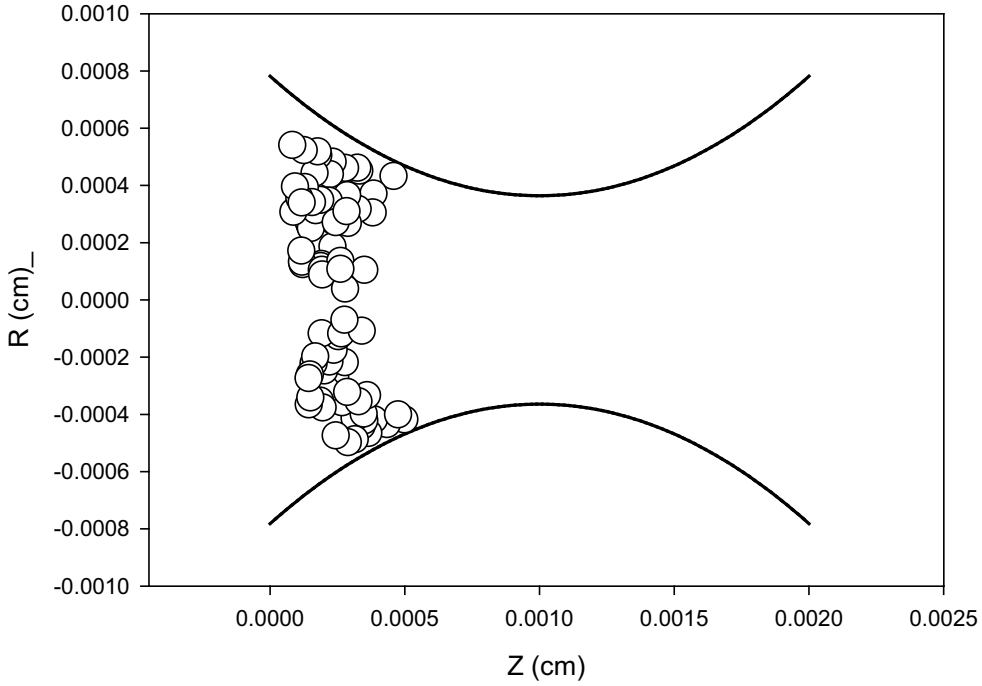
0.0010
0.0008
0.0006
0.0004
0.0002
0.0000
-0.0002
-0.0004
-0.0006
-0.0008
-0.0010
R (cm)_
0.0000
0.0005
0.0010
0.0015
0.0020
0.0025
Z (cm)

Fig. 4(b)

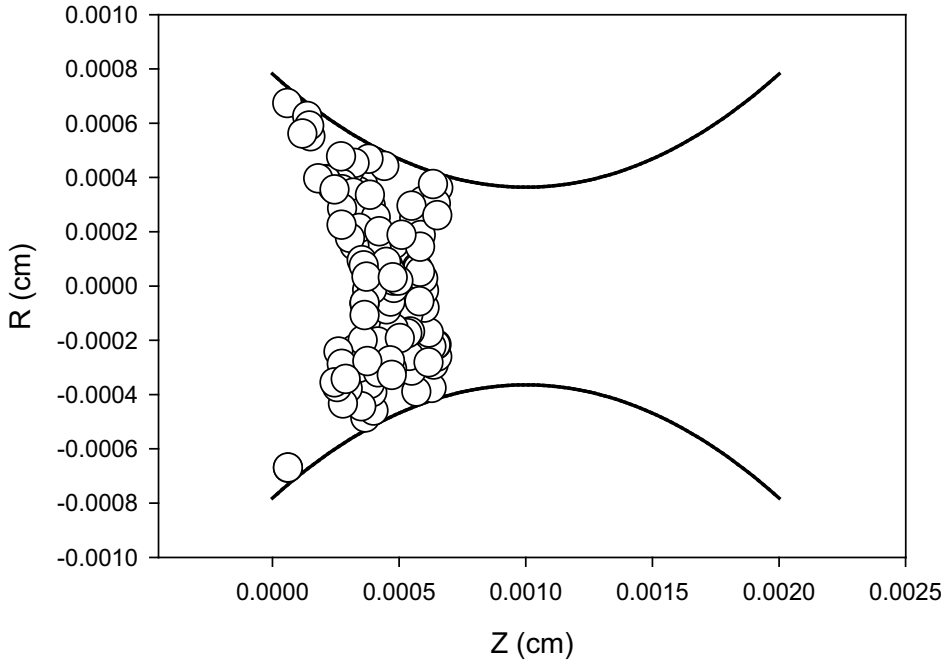
0.0010
0.0008
0.0006
0.0004
0.0002
0.0000
-0.0002
-0.0004
-0.0006
-0.0008
-0.0010
R (cm)
0.0000
0.0005
0.0010
0.0015
0.0020
0.0025
Z (cm)

Fig. 4(c)

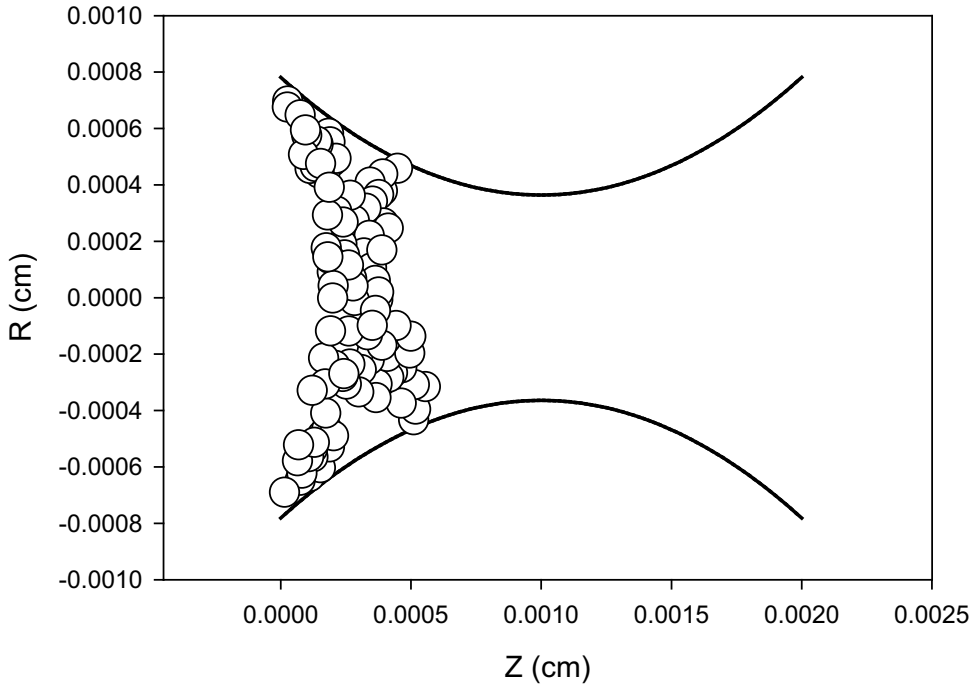
0.0010
0.0008
0.0006
0.0004
0.0002
0.0000
-0.0002
-0.0004
-0.0006
-0.0008
-0.0010
R (cm)
0.0000
0.0005
0.0010
0.0015
0.0020
0.0025
Z (cm)

Fig. 4(d)

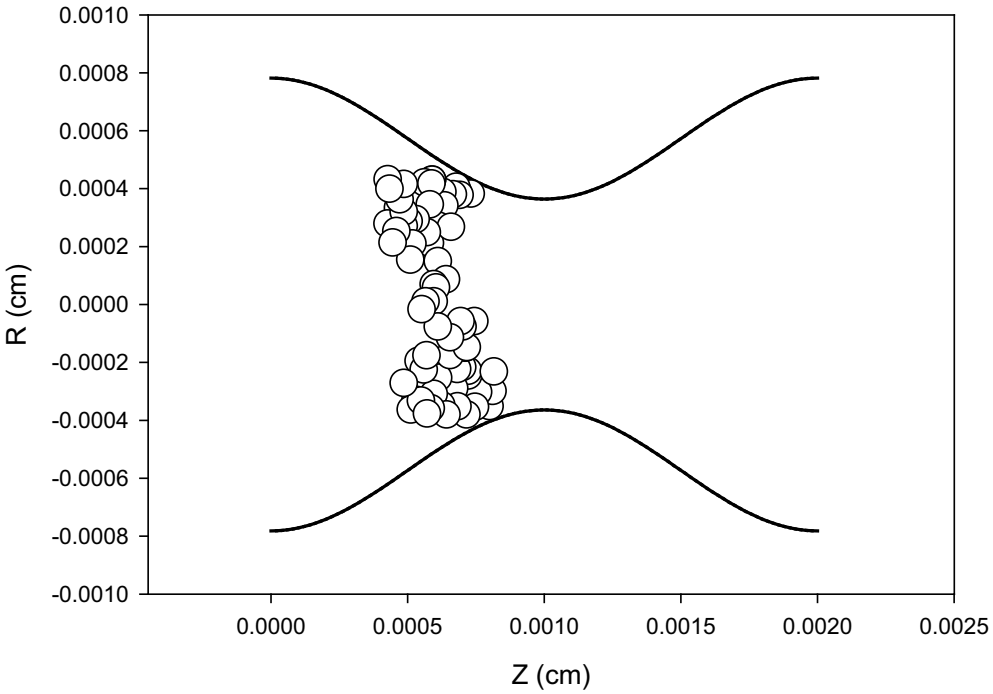
0.0010
0.0008
0.0006
0.0004
0.0002
0.0000
-0.0002
-0.0004
-0.0006
-0.0008
-0.0010
R (cm)
0.0000
0.0005
0.0010
0.0015
0.0020
0.0025
Z (cm)

Fig. 5(a)

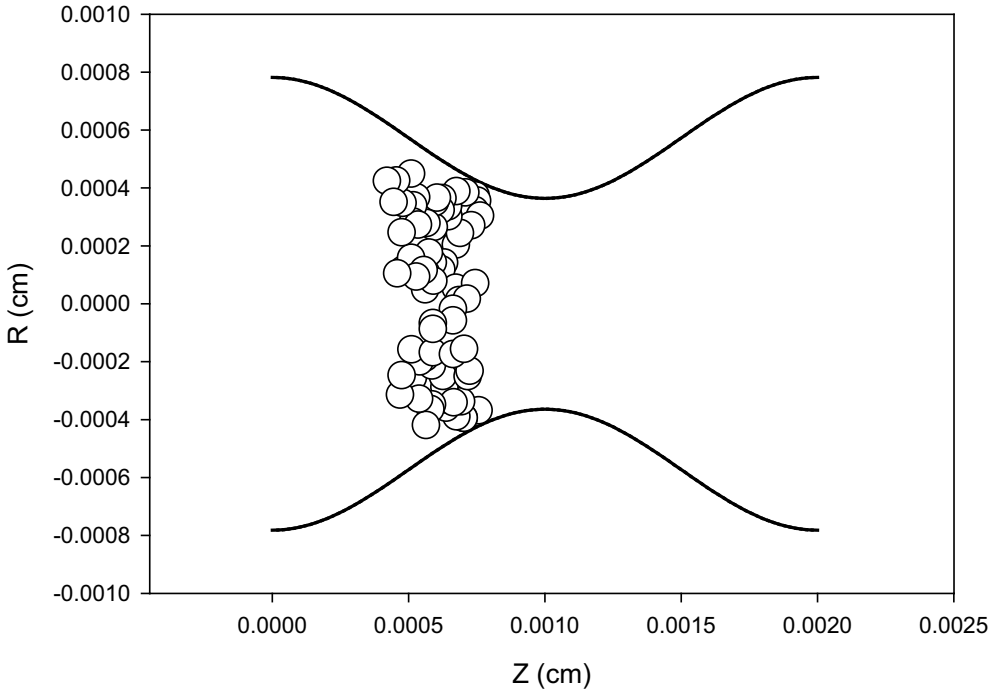
0.0010
0.0008
0.0006
0.0004
0.0002
0.0000
-0.0002
-0.0004
-0.0006
-0.0008
-0.0010
R (cm)
0.0000
0.0005
0.0010
0.0015
0.0020
0.0025
Z (cm)

Fig. 5(b)

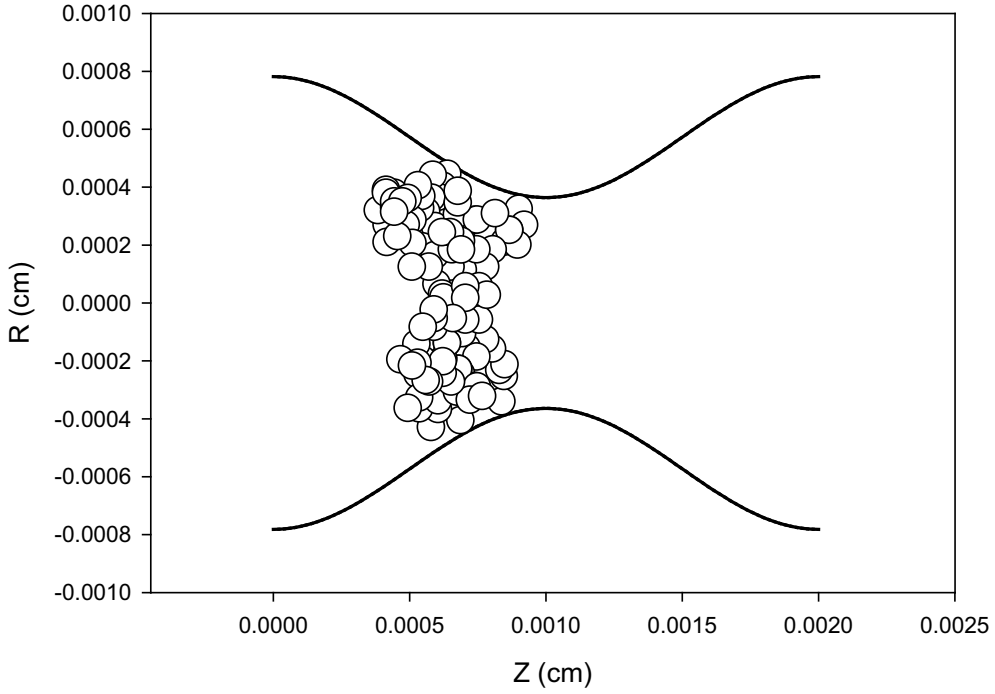
0.0010
0.0008
0.0006
0.0004
0.0002
0.0000
-0.0002
-0.0004
-0.0006
-0.0008
-0.0010
R (cm)
0.0000
0.0005
0.0010
0.0015
0.0020
0.0025
Z (cm)

Fig. 5(c)

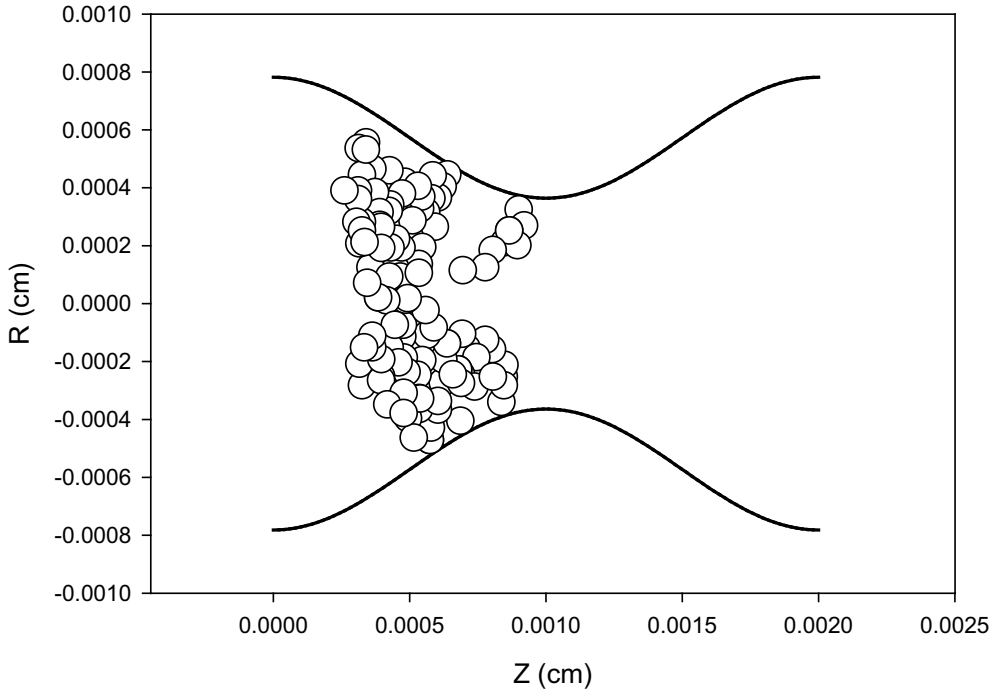
0.0010
0.0008
0.0006
0.0004
0.0002
0.0000
-0.0002
-0.0004
-0.0006
-0.0008
-0.0010
R (cm)
0.0000
0.0005
0.0010
0.0015
0.0020
0.0025
Z (cm)

Fig. 5(d)

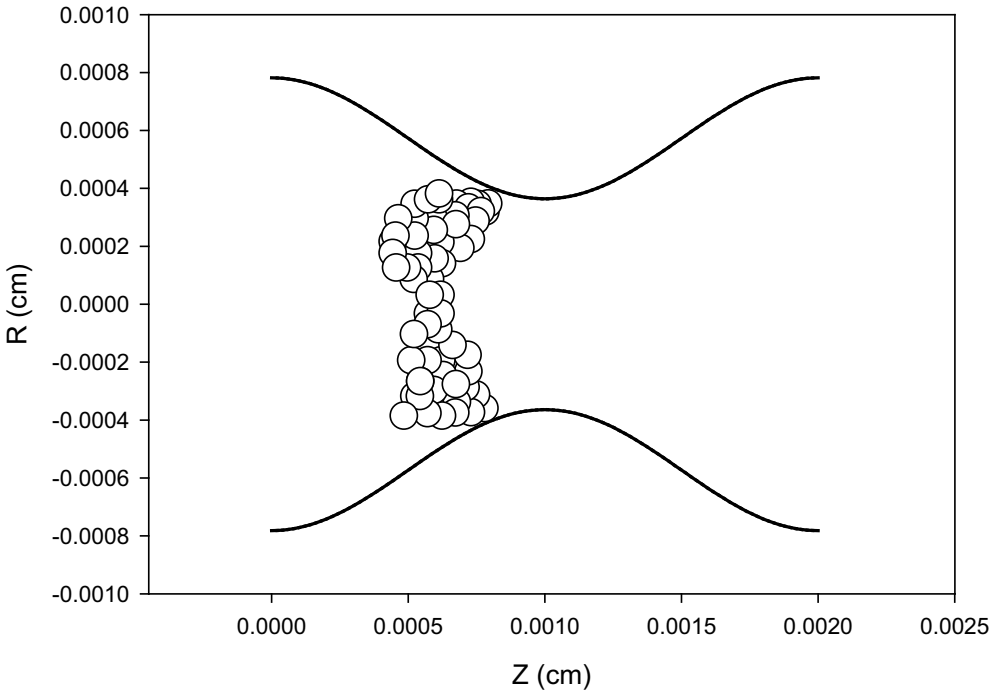
0.0010
0.0008
0.0006
0.0004
0.0002
0.0000
-0.0002
-0.0004
-0.0006
-0.0008
-0.0010
R (cm)
0.0000
0.0005
0.0010
0.0015
0.0020
0.0025
Z (cm)

Fig. 6(a)

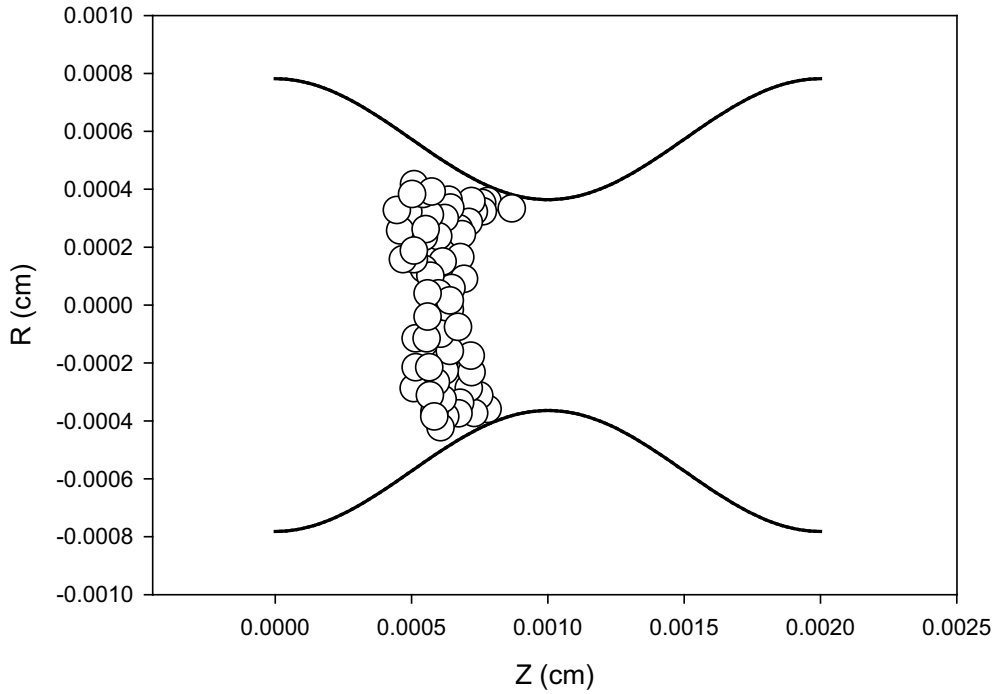
0.0010
0.0008
0.0006
0.0004
0.0002
0.0000
-0.0002
-0.0004
-0.0006
-0.0008
-0.0010
R (cm)
0.0000
0.0005
0.0010
0.0015
0.0020
0.0025
Z (cm)

Fig. 6(b)

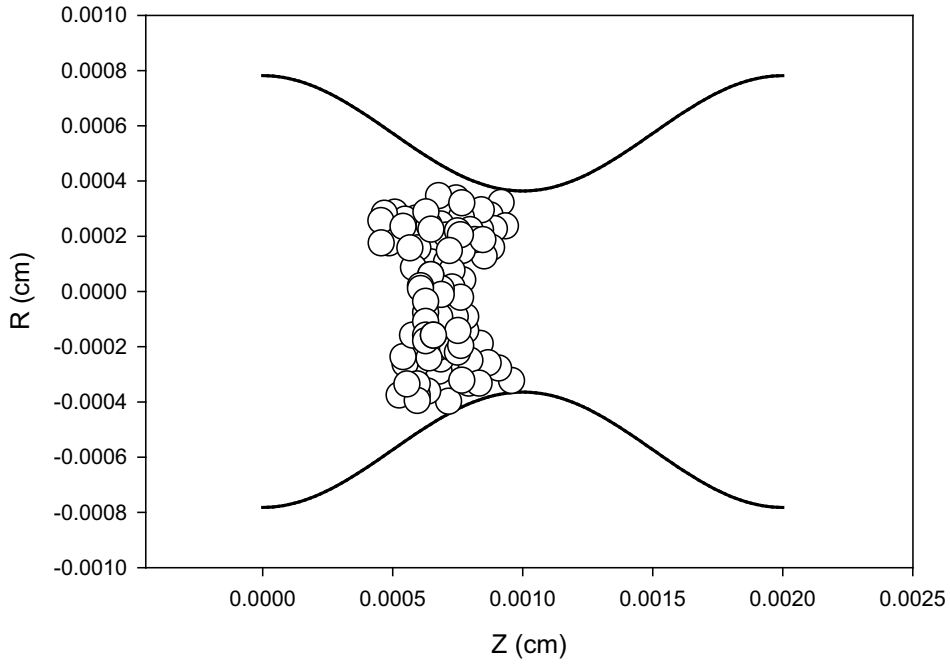
0.0010
0.0008
0.0006
0.0004
0.0002
0.0000
-0.0002
-0.0004
-0.0006
-0.0008
-0.0010
R (cm)
0.0000
0.0005
0.0010
0.0015
0.0020
0.0025
Z (cm)

Fig. 6(c)

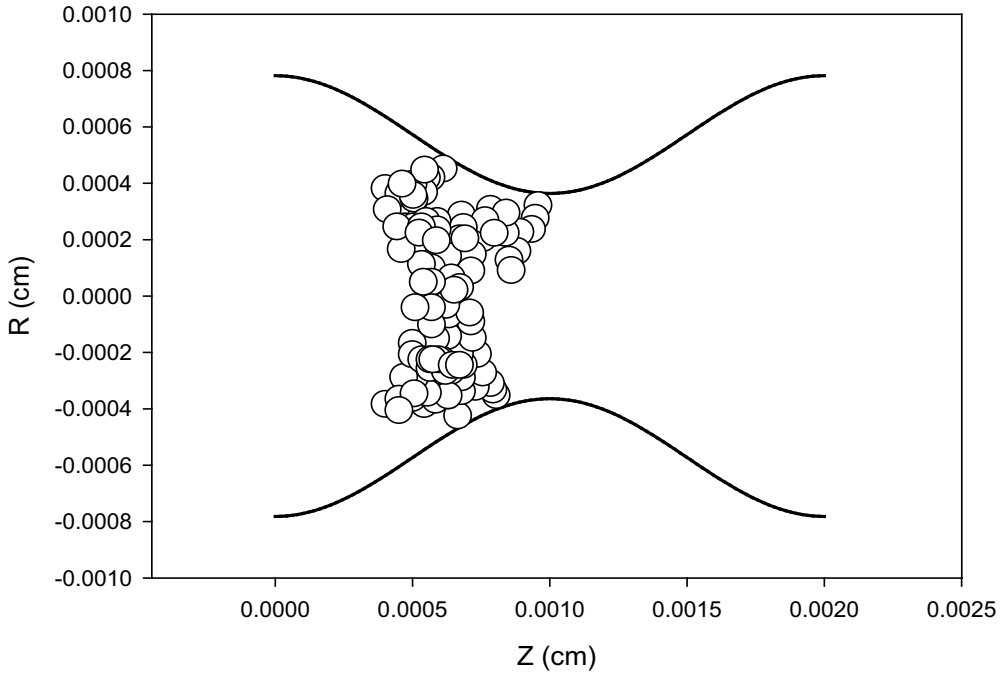
0.0010
0.0008
0.0006
0.0004
0.0002
0.0000
-0.0002
-0.0004
-0.0006
-0.0008
-0.0010
R (cm)
0.0000
0.0005
0.0010
0.0015
0.0020
0.0025
Z (cm)

Fig. 6(d)

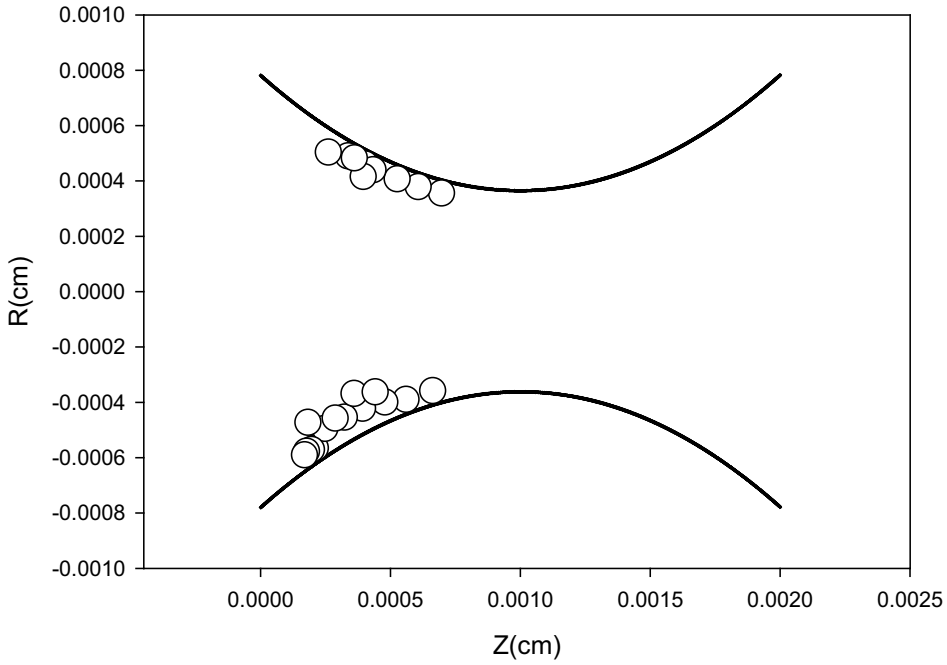
0.0010
0.0008
0.0006
0.0004
0.0002
0.0000
-0.0002
-0.0004
-0.0006
-0.0008
-0.0010
R(cm)
0.0000
0.0005
0.0010
0.0015
0.0020
0.0025
Z(cm)

Fig. 7(a)

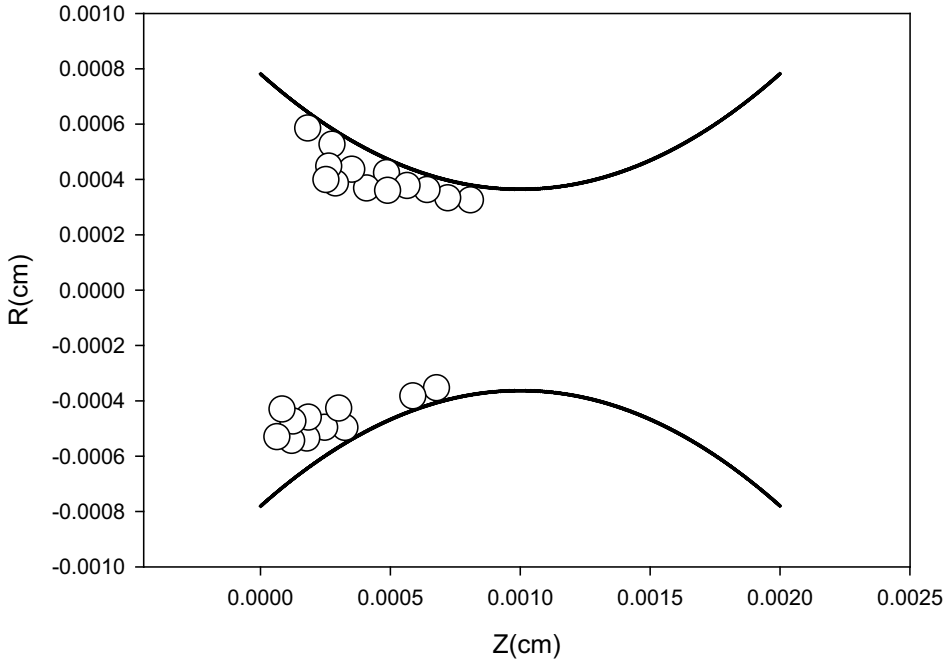
0.0010
0.0008
0.0006
0.0004
0.0002
0.0000
-0.0002
-0.0004
-0.0006
-0.0008
-0.0010
R(cm)
0.0000
0.0005
0.0010
0.0015
0.0020
0.0025
Z(cm)

Fig. 7(b)

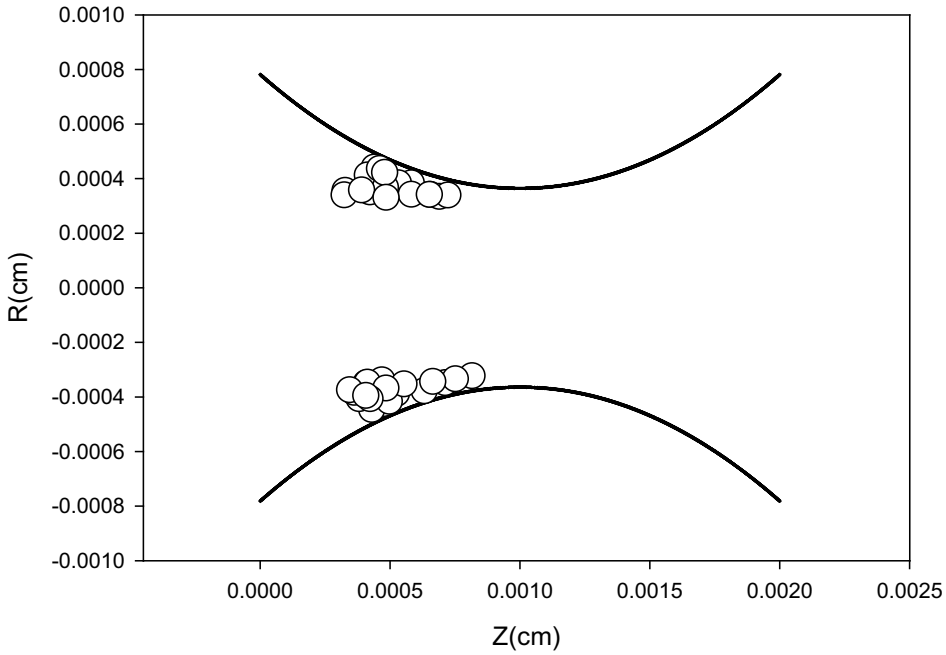
0.0010
0.0008
0.0006
0.0004
0.0002
0.0000
-0.0002
-0.0004
-0.0006
-0.0008
-0.0010
R(cm)
0.0000
0.0005
0.0010
0.0015
0.0020
0.0025
Z(cm)

Fig. 7(c)

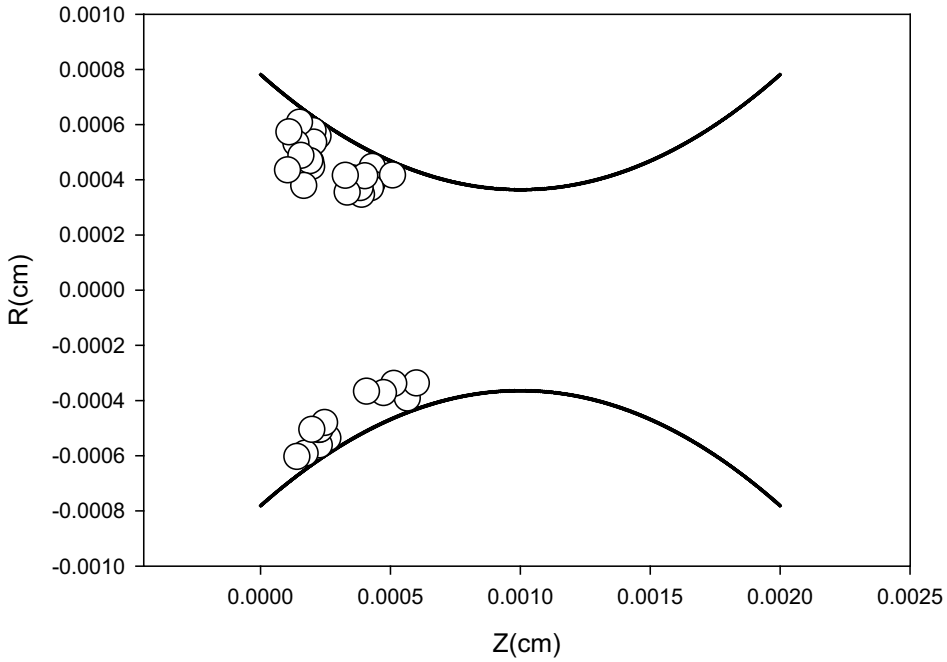
0.0010
0.0008
0.0006
0.0004
0.0002
0.0000
-0.0002
-0.0004
-0.0006
-0.0008
-0.0010
R(cm)
0.0000
0.0005
0.0010
0.0015
0.0020
0.0025
Z(cm)

Fig. 7(d)

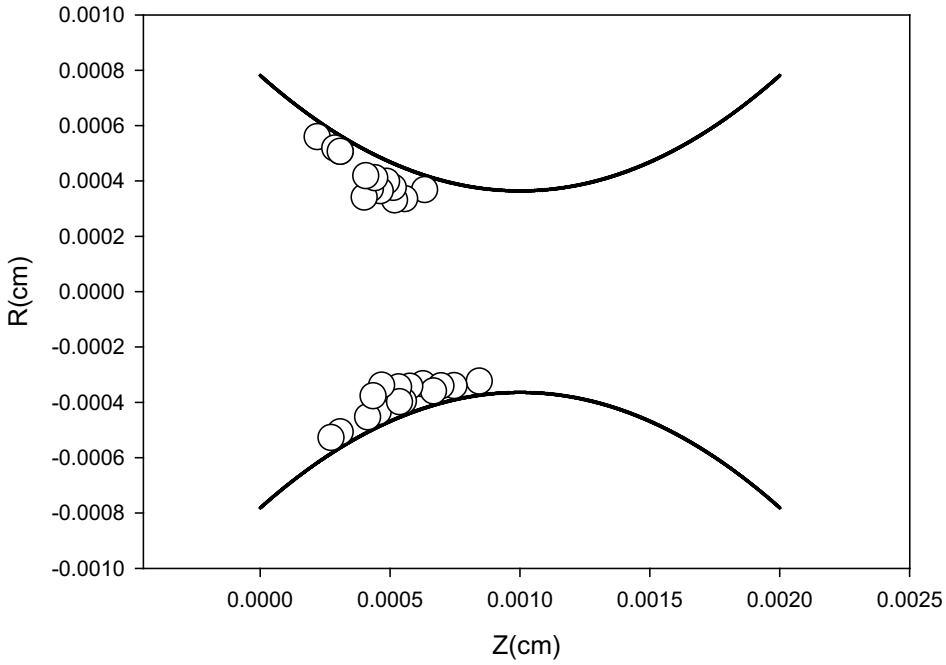
0.0010
0.0008
0.0006
0.0004
0.0002
0.0000
-0.0002
-0.0004
-0.0006
-0.0008
-0.0010
R(cm)
0.0000
0.0005
0.0010
0.0015
0.0020
0.0025
Z(cm)

Fig. 8(a)

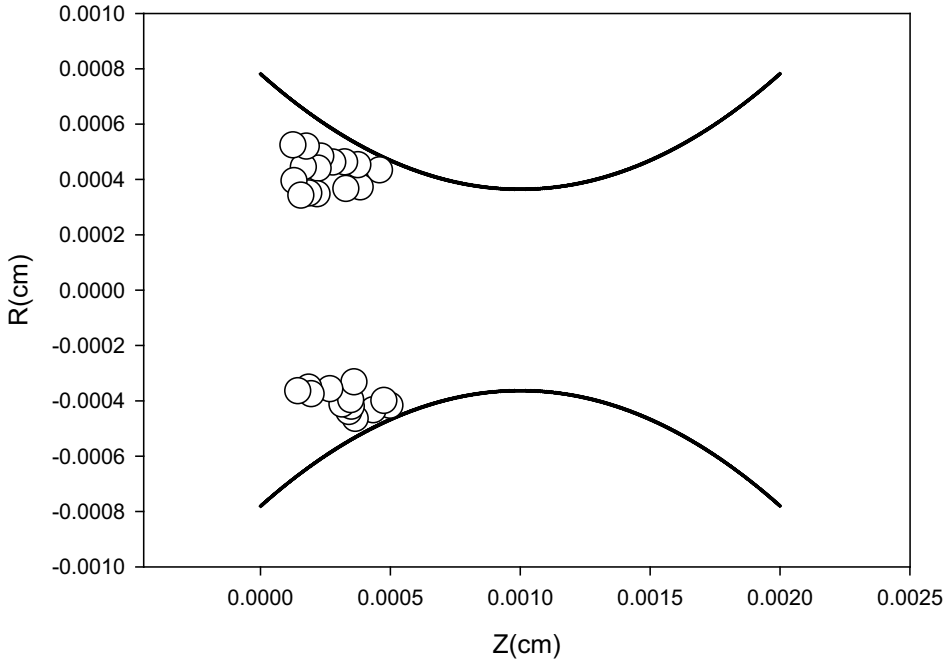
0.0010
0.0008
0.0006
0.0004
0.0002
0.0000
-0.0002
-0.0004
-0.0006
-0.0008
-0.0010
R(cm)
0.0000
0.0005
0.0010
0.0015
0.0020
0.0025
Z(cm)

Fig. 8(b)

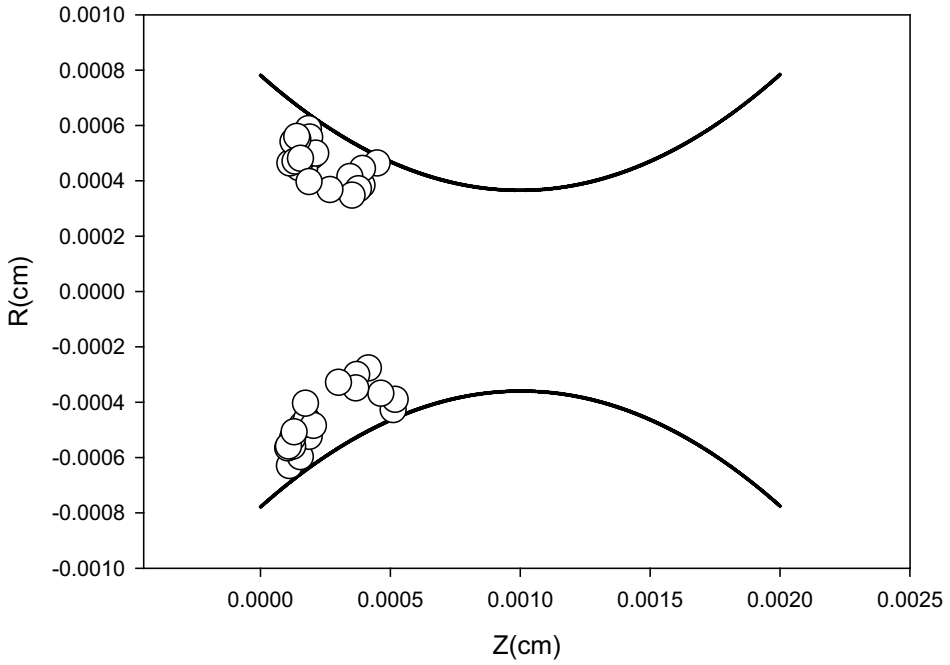
0.0010
0.0008
0.0006
0.0004
0.0002
0.0000
-0.0002
-0.0004
-0.0006
-0.0008
-0.0010
R(cm)
0.0000
0.0005
0.0010
0.0015
0.0020
0.0025
Z(cm)

Fig. 8(c)

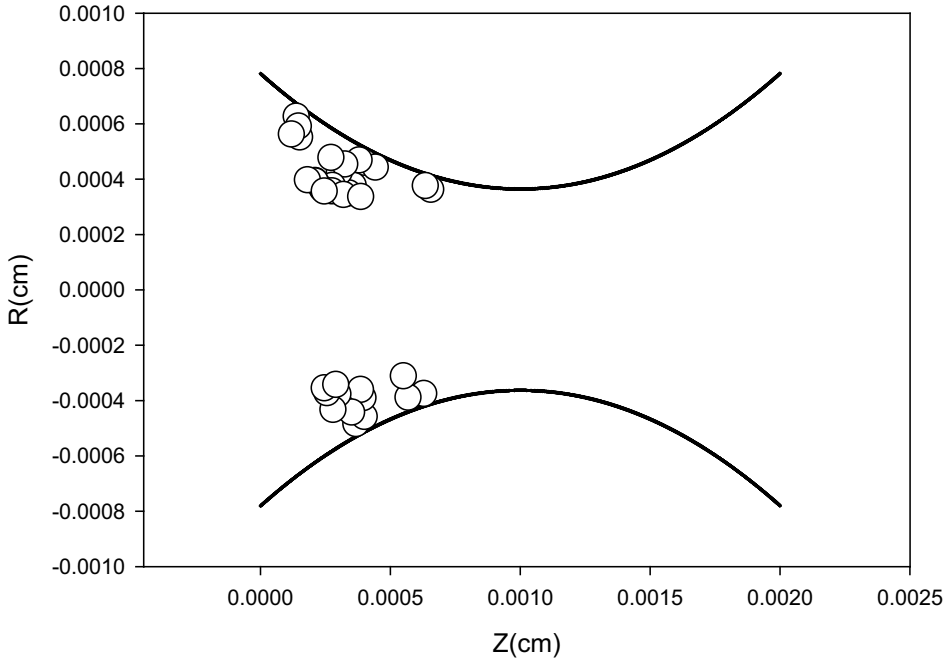
0.0010
0.0008
0.0006
0.0004
0.0002
0.0000
-0.0002
-0.0004
-0.0006
-0.0008
-0.0010
R(cm)
0.0000
0.0005
0.0010
0.0015
0.0020
0.0025
Z(cm)

Fig. 8(d)

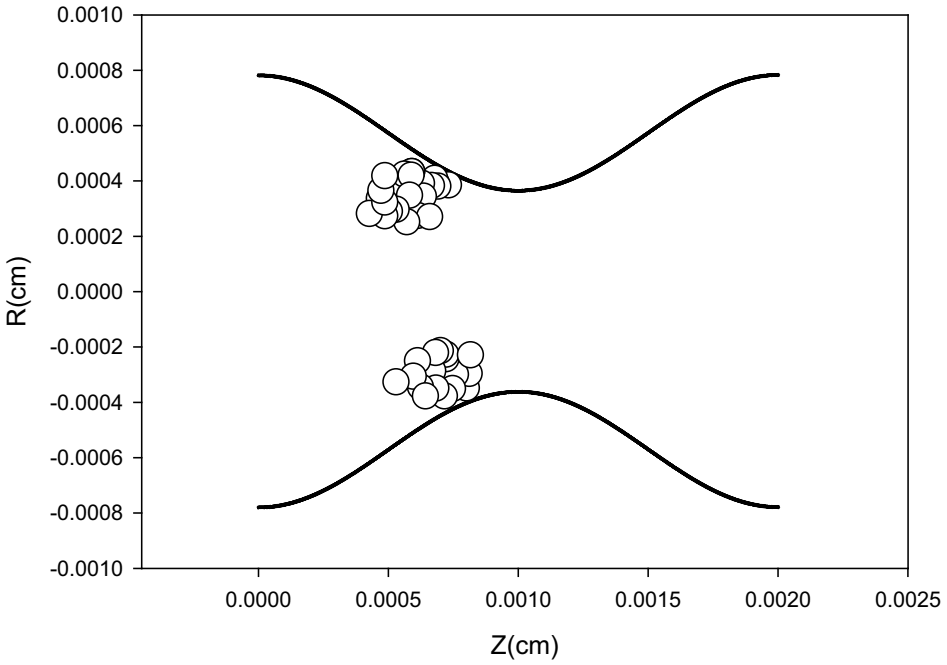
0.0010
0.0008
0.0006
0.0004
0.0002
0.0000
-0.0002
-0.0004
-0.0006
-0.0008
-0.0010
R(cm)
0.0000
0.0005
0.0010
0.0015
0.0020
0.0025
Z(cm)

Fig. 9(a)

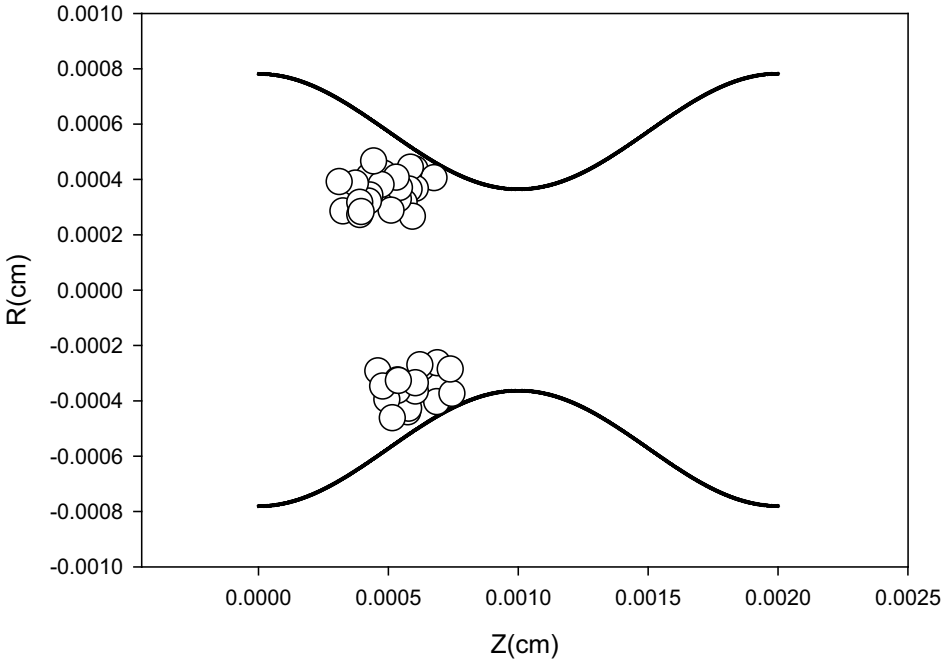
0.0010
0.0008
0.0006
0.0004
0.0002
0.0000
-0.0002
-0.0004
-0.0006
-0.0008
-0.0010
R(cm)
0.0000
0.0005
0.0010
0.0015
0.0020
0.0025
Z(cm)

Fig. 9(b)

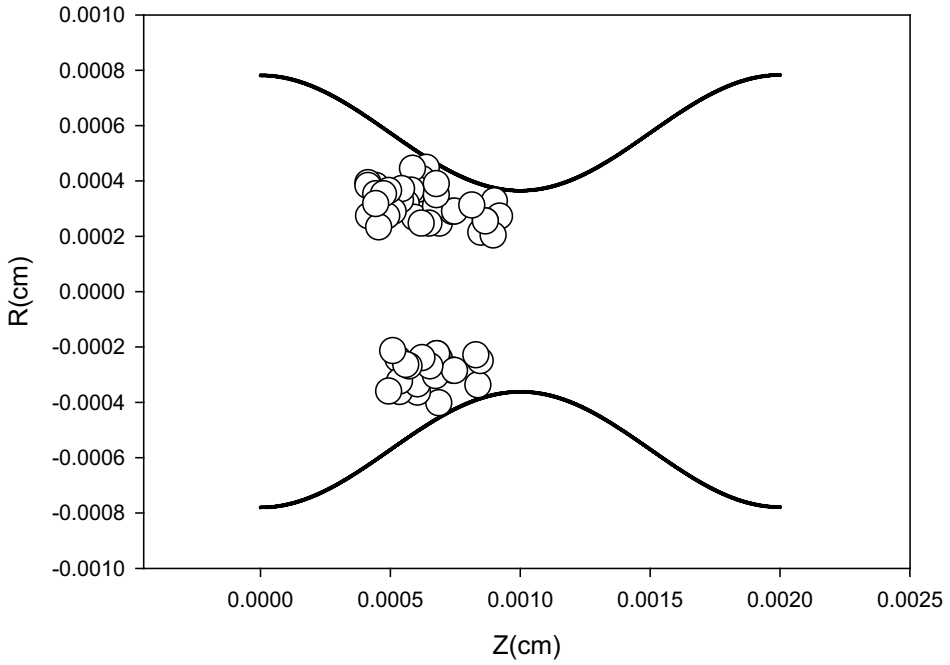
0.0010
0.0008
0.0006
0.0004
0.0002
0.0000
-0.0002
-0.0004
-0.0006
-0.0008
-0.0010
R(cm)
0.0000
0.0005
0.0010
0.0015
0.0020
0.0025
Z(cm)

Fig. 9(c)

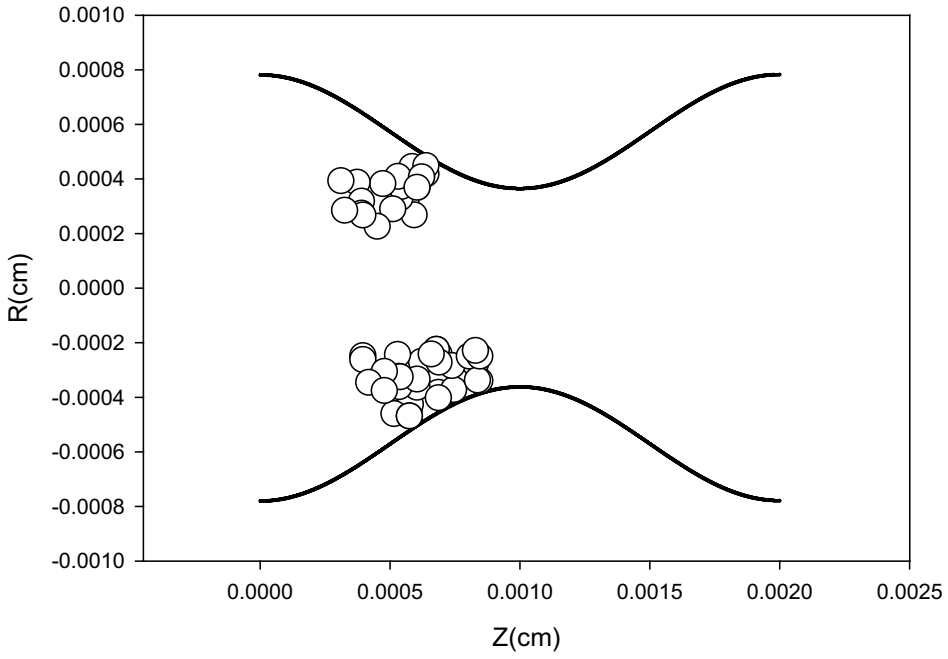
0.0010
0.0008
0.0006
0.0004
0.0002
0.0000
-0.0002
-0.0004
-0.0006
-0.0008
-0.0010
R(cm)
0.0000
0.0005
0.0010
0.0015
0.0020
0.0025
Z(cm)

Fig. 9(d)

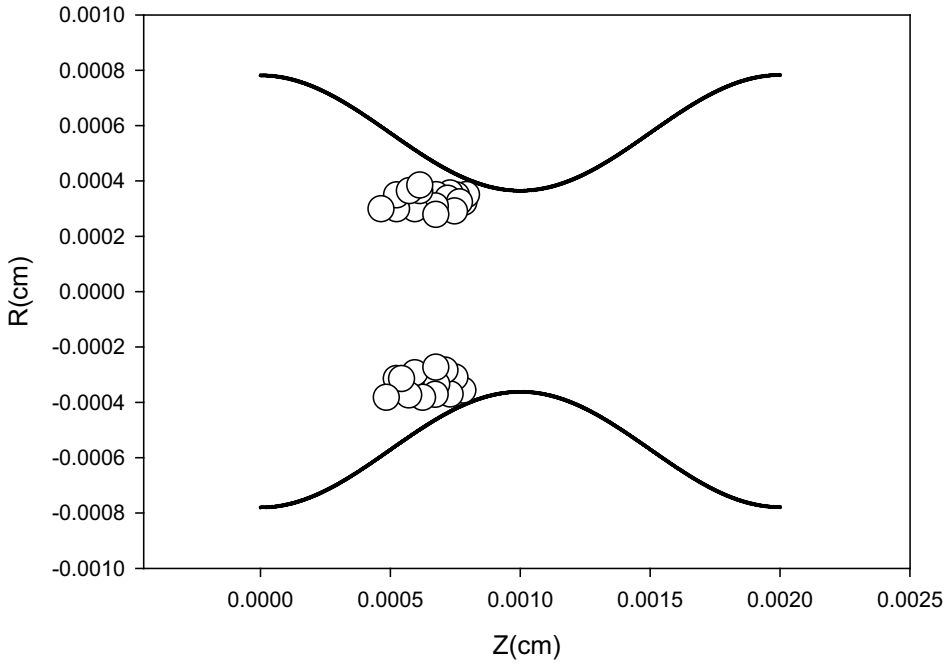

Fig. 10(a)

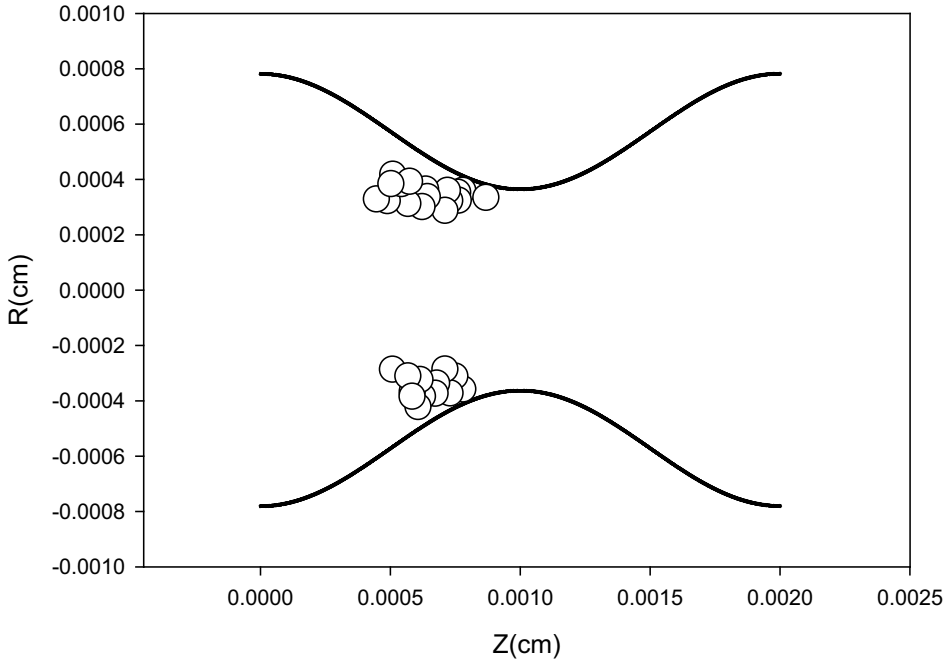

Fig. 10(b)

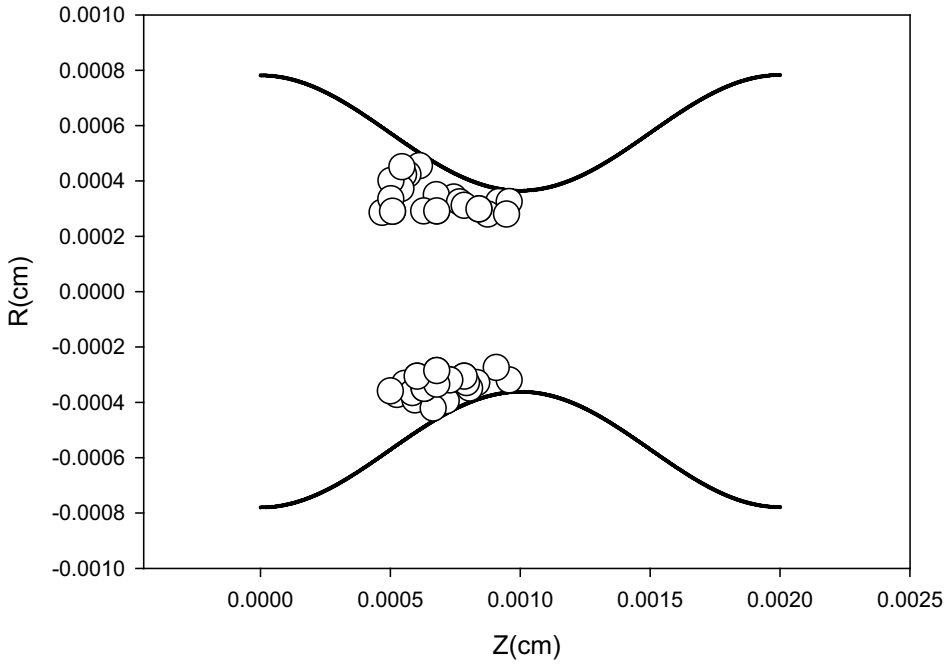

Fig. 10(c)

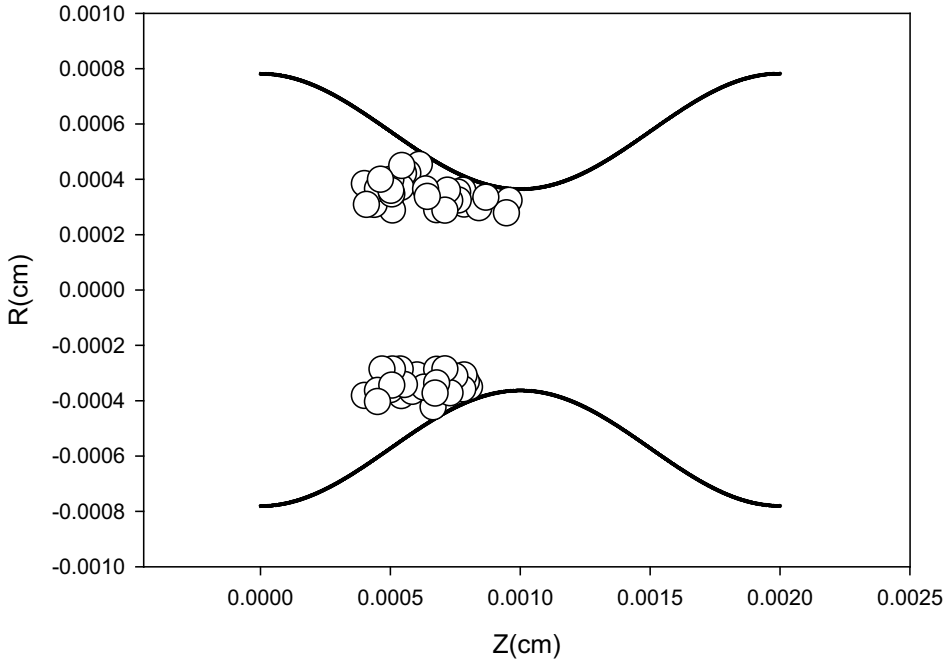

Fig. 10(d)